Hindawi
Shock and Vibration
Volume 2021, Article ID 5806444, 20 pages
https://doi.org/10.1155/2021/5806444

Research Article

Study of Suspension Parameters Matching to Enhance Vehicle Ride Comfort on Bump Road

Jin Gao and Xiaoping Qi

Faculty of Transportation Engineering, Kunming University of Science and Technology, Kunming 650500, China

Correspondence should be addressed to Jin Gao; 906845822@qq.com

Received 1 November 2021; Revised 10 November 2021; Accepted 15 November 2021; Published 16 December 2021

Academic Editor: Mohamed A. A. Abdelkareem

In this study, the parameters of the MacPherson front suspension and the E-type multilink rear suspension are matched to enhance the vehicle ride comfort on bump road. Vehicle vibration and suspension stiffness are analyzed theoretically. In the simulation study, the influence of the front and rear wheels on the vehicle vibration is considered, so the time-domain curves of the front and rear seat rail accelerations are processed by adding windows with two different window functions. The resulting $\Delta RmsLocal$ and $\Delta RmsGlobal$ are used as evaluation indexes of the vehicle ride comfort. The sensitivity analysis yields the magnitude of the influence of the suspension parameters on the evaluation indexes. In addition, the trends of $\Delta RmsLocal$ and $\Delta RmsGlobal$ with bushing stiffness at different vehicle speeds are discussed. The results show that longitudinal $\Delta RmsLocal$ and $\Delta RmsGlobal$ of the seat rails are influenced by the bushings mostly, while the vertical $\Delta RmsLocal$ and $\Delta RmsGlobal$ of the seat rails are influenced by the spring and shock absorber mostly. The trends of $\Delta RmsLocal$ and $\Delta RmsGlobal$ with bushing stiffness are influenced by the speed of the vehicle. Finally, the vehicle ride comfort is enhanced after optimization and matching of the suspension parameters by NSGA-II optimization algorithm.

1. Introduction

Vehicle ride comfort refers to keeping the impact of vibrations and shocks within certain ranges when the vehicle is excited by the road. The study of vehicle ride comfort has always been a subject of interest for scholars.

Several scholars have carried out extensive theoretical studies on vehicle ride comfort [1–5]. Wang et al. [1] developed a frequency-based modelling approach for vehicles equipped with a hydraulic interconnected suspension (HIS) system. Guntur et al. [2] focused on the effect of the asymmetric characteristics of the damping forces on the ride comfort of a typical passenger car under different road excitations. Jiao et al. [4] proposed a 4-DOF dynamic model for the two-axle heavy truck to investigate the low-frequency vibration characteristics of the suspension system. Zhao et al. [6] established a vibration simulation model of a three-axle goods vehicle passing through a speed bump. The vibration characteristics of the vehicle at different speeds were studied through the simulation, the vibration decay time at different speeds was obtained, and the minimum distance between the speed bump and the vehicle scale was determined.

Several scholars have conducted a lot of studies to improve vehicle ride comfort [7–20]. Qi et al. [8] proposed a new type of suspension including a hydraulically interlinked suspension and electronically controlled air springs, enabling a high level of performance in terms of both handling stability and ride comfort. Tan et al. [9] proposed a pitch-roll-interconnected hydropneumatic suspension system to improve the stability and attenuate the vibration for the lying patients. Ebrahimi-Nejad et al. [10] derived the vibration control equations for the vehicle suspension system and compared the effects of different damping coefficients and spring stiffnesses on the vehicle ride comfort. Finally, multiobjective optimization was carried out with the TOPSIS method to improve the ride comfort of the vehicle. Li et al. [11] developed a 10-DOF model considering the lying patient

and the driver to investigate the ride comfort of the ambulance. After multiobjective optimization, vehicle ride comfort bump and random road have been improved. Kaldas et al. [12] developed a novel optimization technique for optimizing the damper top mount characteristics to improve vehicle ride comfort. Based on the Bolza-Meyer criterion, Phu [17] proposed a new optimal control law with sliding mode control. The proposed controller is applied to a vehicle seat suspension system with magneto-rheological damper to evaluate vibration control performances. Through simulation studies, the proposed optimal controller is shown to have the advantages of less power and faster convergence. He et al. [18] developed and simulated a multibody dynamics model based on nonlinear damping and equivalent damping and optimized with an optimization method based on nonlinear damping and intelligent algorithms to improve the vehicle ride comfort. Phu et al. [19] designed a new controller based on a modified Riccati-like equation. Simulation experiments are carried out on both bump and random road. The results show that the controller can control the acceleration and displacement at the driver position effectively. Phu et al. [20] proposed a novel adaptive control method to deal with the dead zone and time delay issues in actuators of vibration control systems. The unwanted vibrations due to external excitations are well controlled despite of the presence of dead zone and time delay in actuators.

Many studies by scholars have focused on the vibration of vehicles on random road. Global and local vibrations are not considered separately in the study of vibration characteristics. Most of the studies improve vehicle ride comfort only by matching spring stiffness of suspension and damping coefficient of shock absorber. The optimization of vehicle ride comfort based on specific suspension structures has not yet been well explored.

This study takes into account the following aspects: (a) taking a full vehicle model with a MacPherson front suspension and an E-type multilink rear suspension as an example, the influence of the bushing is analyzed from a force perspective, and the contribution of bushing stiffness to suspension stiffness is discussed. (b) The vehicle is simulated on bump road. Local and global vibrations are considered, so the time-domain curves of the front and rear seat rails are windowing with different window functions and the resulting $\Delta RmsLocal$ and $\Delta RmsGlobal$ are used as evaluation indexes. (c) Sensitivity analysis resulted in the most influential suspension parameters for $\Delta RmsLocal$ and $\Delta RmsGlobal$. The conclusions resulting from the theoretical analysis are verified. The trend of $\Delta RmsLocal$ and $\Delta RmsGlobal$ with bushing stiffness is further discussed. (d) Considering the coupling of the full vehicle vibration, the suspension parameters are matched reasonably at different vehicle speeds using the NSGA-II algorithm.

The paper is organized as follows: Section 2 develops a vehicle vibration model and discusses the ride comfort characteristics of the vehicle. Section 3 analyzes the influence of suspension's parameters on suspension's stiffness. Section 4 verifies the conclusions from part two and part three through simulation. In Section 5, the front and rear suspension parameters are matched by an optimization algorithm to improve the ride comfort of the vehicle. Section 6 presents the conclusions of this study.

2. Vehicle Vibration Characteristics Analysis

2.1. Vertical Longitudinal Vibration Model. Road excitation may cause vertical, pitch, and longitudinal vibrations of the vehicle. The vertical longitudinal coupling model [21] is shown in Figure 1. The model consists of sprung mass represented by the body m_b, unsprung mass represented by the front axle and wheel m_1, rear axle, and wheel m_2. There is relative vertical and longitudinal movement between the body and the wheels. The body can pitch around the y axes, I_y representing the pitch inertia of the body around the y axe. K_{eqfz} and K_{eqrz} are the vertical equivalent stiffnesses of the front and rear suspensions, respectively; K_{eqfx} and K_{eqrx} are the longitudinal equivalent stiffnesses of the front and rear suspensions, respectively; B_{eqfz} and B_{eqrz} are the vertical equivalent damping coefficients of the front and rear suspensions, respectively; B_{eqfx} and B_{eqr} are the longitudinal equivalent damping coefficients of the front and rear suspensions, respectively; Q is the road excitation; Z_{tf} and Z_{tr} are the vertical displacements of the front and rear wheels, respectively; X_{tf} and X_{tr} are the longitudinal displacements of front and rear wheels, respectively; Z_f and Z_r are the vertical displacements of the front and rear body, respectively; X_f and X_r are the longitudinal displacements of the front and rear body, respectively; Z_b is the vertical displacement at the centre of mass of the body; X_b is the longitudinal displacement at the centre of mass of the body.

Neglecting the damping of the tyres, the forces between the wheels and the body consist of elastic and damping forces. According to the Lagrange equation, which is expressed as shown in equation (1), the equation of vehicle coupling vibration can be derived

$$\frac{\mathrm{d}}{\mathrm{d}t}\left(\frac{\partial L}{\partial \dot{q}_i}\right) - \frac{\partial L}{\partial q_i} = -\frac{\partial R}{\partial \dot{q}_i}, \quad i = 1, 2, 3, \ldots n. \tag{1}$$

L is a Lagrangian function

$$L = T - U, \tag{2}$$

where T, U, and R are the kinetic energy, potential energy, and dissipative energy of the system, respectively.

Generalized coordinates are defined as

$$\left[X_{tf} \;\; X_{tr} \;\; Z_{tf} \;\; Z_{tr} \;\; X_b \;\; Z_b \;\; \varphi \right]. \tag{3}$$

Generalized velocity is defined as

$$\left[\dot{X}_{tf} \;\; \dot{X}_{tr} \;\; \dot{Z}_{tf} \;\; \dot{Z}_{tr} \;\; \dot{X}_b \;\; \dot{Z}_b \;\; \dot{\varphi} \right]. \tag{4}$$

Based on the above analysis of the vehicle model, the potential energy of vehicle vibration can be expressed by the stiffness characteristics of the system

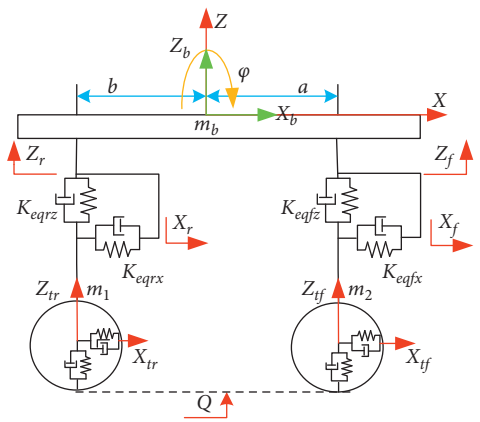

Figure 1: Coupling longitudinal vertical vehicle model.

$$U=\frac{1}{2}\begin{bmatrix} K_{tzf}\left(Z_{tf}-q_{zf}\right)^2+K_{tzr}\left(Z_{tr}-q_{zr}\right)^2+K_{eqf}\left(Z_f-Z_{tf}\right)^2 \\ +K_{eqr}\left(Z_r-Z_{tr}\right)^2+K_{txf}\left(X_{tf}-q_{xf}\right)^2+K_{txr}\left(X_{tr}-q_{xr}\right)^2+ \\ K_{eqf}\left(X_f-X_{tf}\right)^2+K_{eqr}\left(X_r-X_{tr}\right)^2 \end{bmatrix}. \tag{5}$$

The kinetic energy of the vehicle vibration can be found as

$$T=\frac{1}{2}\left(m_b\dot{Z}_b^2+m_b\dot{X}_b^2+I_y\dot{\varphi}^2+m_1\dot{Z}_{tf}^2+m_2\dot{Z}_{tr}^2+m_1\dot{X}_{tf}^2+m_2\dot{X}_{tr}^2\right). \tag{6}$$

The dissipation energy of vehicle vibrations can be expressed by the damping characteristics of the system

$$R=\frac{1}{2}\begin{bmatrix} B_{eqf}\left(\dot{Z}_f-\dot{Z}_{tf}\right)^2+B_{eqr}\left(\dot{Z}_r-\dot{Z}_{tr}\right)^2 \\ +B_{eqf}\left(\dot{X}_f-\dot{X}_{tf}\right)^2+B_{eqr}\left(\dot{X}_r-\dot{X}_{tr}\right)^2 \end{bmatrix}. \tag{7}$$

The geometric constraints of the model satisfy the following equations:

$$\begin{cases} Z_f=Z_b-\left(X_b-X_{tf}+a\right)\varphi, \\ \dot{Z}_f=\dot{Z}_b-\left(X_b-X_{tf}+a\right)\dot{\varphi}, \\ Z_r=Z_b+\left(X_b-X_{tr}+b\right)\varphi, \\ \dot{Z}_r=\dot{Z}_b+\left(X_b-X_{tr}+b\right)\dot{\varphi}, \\ X_f=X_b-\left(Z_b-Z_{tf}+h_{bw}\right)\varphi, \\ \dot{Z}_f=\dot{X}_b-\left(Z_b-Z_{tf}+h_{bw}\right)\dot{\varphi}, \\ X_r=X_b-\left(Z_b-Z_{tr}+h_{bw}\right)\varphi, \\ \dot{Z}_f=\dot{X}_b-\left(Z_b-Z_{tr}+h_{bw}\right)\dot{\varphi}, \end{cases} \tag{8}$$

where h_{bw} is the wheel's centre and vehicle body's centre of gravity when the wheel is not in deformation.

Substituting equations (2) and (5)–(8) into (1) yields the differential equation of vehicle vibration.

$$\begin{cases} m_1\ddot{X}_{tf}+B_{eqfx}\dot{X}_{tf}-B_{eqfx}\dot{X}_b-B_{eqfx}c_1\dot{\varphi}+K_{eqfx}X_{tf}-K_{eqfx}X_b-K_{eqfx}c_1\varphi+K_{txf}\left(X_{tf}-q_{xf}\right)=0, \\ m_2\ddot{X}_{tr}+B_{eqrx}\dot{X}_{tr}-B_{eqrx}\dot{X}_b-B_{eqrx}c_2\dot{\varphi}+K_{eqrx}X_{tr}-K_{eqrx}X_b-K_{eqrx}c_2\varphi+K_{txr}\left(X_{tr}-q_{xr}\right)=0, \\ m_1\ddot{Z}_{tf}+B_{eqfz}\dot{Z}_{tf}-B_{eqfz}\dot{Z}_b+B_{eqfz}b_1\dot{\varphi}+K_{eqfz}Z_{tf}-K_{eqfz}Z_b+K_{eqfz}b_1\varphi+K_{tzf}\left(Z_{tf}-q_{zf}\right)=0, \\ m_2\ddot{Z}_{tr}+B_{eqrz}\dot{Z}_{tr}-B_{eqrz}\dot{Z}_b-B_{eqrz}b_2\dot{\varphi}+K_{eqrz}Z_{tr}-K_{eqrz}Z_b-K_{eqrz}b_2\varphi+K_{tzr}\left(Z_{tr}-q_{zr}\right)=0, \\ m_b\ddot{X}_b+\left(B_{eqfx}+B_{eqfx}\right)\dot{X}_b-\left(B_{eqfx}c_1+B_{eqrx}c_2\right)\dot{\varphi}-B_{eqfx}\dot{X}_{tf}-B_{eqrx}\dot{X}_{tr}+\left(K_{eqfx}+K_{eqrx}\right)X_b \\ -\left[K_{eqfx}c_1+K_{eqrx}c_2\right]\varphi-K_{eqfx}X_{tf}-K_{eqrx}X_{tr}=0, \\ m_b\ddot{Z}_b+\left(B_{eqfz}+B_{eqfz}\right)\dot{Z}_b+\left[B_{eqrz}b_2-B_{eqfz}b_1\right]\dot{\varphi}-B_{eqfz}\dot{Z}_{tf}-B_{eqrz}\dot{Z}_{tr}+\left(K_{eqfz}+K_{eqrz}\right)Z_b \\ +\left[K_{eqrz}b_2-K_{eqfz}b_2\right]\varphi-K_{eqfz}Z_{tf}-K_{eqrz}Z_{tr}=0, \\ I_y\ddot{\varphi}+\left[B_{eqfz}b_1^2+B_{eqrz}b_2^2+B_{eqfx}c_1^2+B_{eqrx}c_2^2\right]\dot{\varphi}+\left[B_{eqrz}\left(\dot{Z}_b-\dot{Z}_{tr}\right)b_2-B_{eqfz}\left(\dot{Z}_b-\dot{Z}_{tf}\right)b_1\right] \\ +\left[B_{eqfx}\left(\dot{X}_{tf}-\dot{X}_b\right)c_1+B_{eqrx}\left(\dot{X}_{tr}-\dot{X}_b\right)c_2\right]+\left[K_{eqfz}b_1^2+K_{eqrz}b_2^2+K_{eqfx}c_1^2+K_{eqrx}c_2^2\right]\varphi \\ +\left[K_{eqrz}\left(Z_b-Z_{tr}\right)b_2-K_{eqfz}\left(Z_b-Z_{tf}\right)b_1\right]+\left[K_{eqfx}\left(X_{tf}-X_b\right)c_1+K_{eqrx}\left(X_{tr}-X_b\right)c_2\right]=0, \end{cases} \tag{9}$$

where

$$\begin{cases} b_1 = X_b - X_{tf} + a, \\ b_2 = X_b - X_{tr} + b, \\ c_1 = Z_b - Z_{tf} + h_{bw}, \\ c_2 = Z_b - Z_{tr} + h_{bw}. \end{cases} \tag{10}$$

Writing (9) in matrix form yields

$$M\ddot{P} + C\dot{P} + KP = K_t Q, \tag{11}$$

where M is the mass matrix; K is the stiffness matrix; C is the damping matrix; and K_t is the stiffness matrix of the tyre.

$$\begin{aligned} M &= \operatorname{diag}\begin{pmatrix} m_1 & m_2 & m_1 & m_2 & m_b & m_b & I_y \end{pmatrix}, \\ K &= \begin{bmatrix} K_{eqfx} & 0 & 0 & 0 & -K_{eqfx} & 0 & -K_{eqfx}c_1 \\ 0 & K_{eqrx} & 0 & 0 & -K_{eqrx} & 0 & -K_{eqrx}c_2 \\ 0 & 0 & K_{eqfz} & 0 & 0 & -K_{eqfz} & K_{eqfz}b_1 \\ 0 & 0 & 0 & K_{eqrz} & 0 & -K_{eqrz} & -K_{eqrz}b_2 \\ -K_{eqfx} & -K_{eqrx} & 0 & 0 & K_{eqfx} + K_{eqfx} & 0 & -\left(K_{eqfx}c_1 + K_{eqrx}c_2\right) \\ 0 & 0 & 0 & 0 & 0 & K_{eqfz} + K_{eqfz} & K_{eqrz}b_2 - K_{eqfz}b_1 \\ K_{eqfx}c_1 & K_{eqrx}c_2 & K_{eqfz}b_1 & -K_{eqrz}b_2 & -K_{eqfx}c_1 - K_{eqrx}c_2 & K_{eqrz}b_2 - K_{eqfz}b_1 & K_{eqfz}b_1^2 + K_{eqrz}b_2^2 + K_{eqfx}c_1^2 + K_{eqrx}c_2^2 \end{bmatrix}, \\ C &= \begin{bmatrix} B_{eqfx} & 0 & 0 & 0 & -B_{eqfx} & 0 & -B_{eqfx}c_1 \\ 0 & B_{eqrx} & 0 & 0 & -B_{eqrx} & 0 & -B_{eqrx}c_2 \\ 0 & 0 & B_{eqfz} & 0 & 0 & -B_{eqfz} & B_{eqfz}b_1 \\ 0 & 0 & 0 & B_{eqrz} & 0 & -B_{eqrz} & -B_{eqrz}b_2 \\ -B_{eqfx} & -B_{eqrx} & 0 & 0 & B_{eqfx} + B_{eqfx} & 0 & -\left(B_{eqfx}c_1 + B_{eqrx}c_2\right) \\ 0 & 0 & 0 & 0 & 0 & B_{eqfz} + B_{eqfz} & B_{eqrz}b_2 - B_{eqfz}b_1 \\ B_{eqfx}c_1 & B_{eqrx}c_2 & B_{eqfz}b_1 & -B_{eqrz}b_2 & -B_{eqfx}c_1 - B_{eqrx}c_2 & B_{eqrz}b_2 - B_{eqfz}b_1 & B_{eqfz}b_1^2 + B_{eqrz}b_2^2 + B_{eqfx}c_1^2 + B_{eqrx}c_2^2 \end{bmatrix}, \\ K_t &= \begin{bmatrix} K_{txf} & K_{txr} & K_{tzf} & K_{tzr} & 0 & 0 & 0 \end{bmatrix}^T. \end{aligned} \tag{12}$$

A Laplace variation of equation (11) yields the transfer function matrix of the system vibration

$$[G(s)] = \left[Ms^2 + Cs + K\right]^{-1}[K_t]. \tag{13}$$

Substituting $s = j\omega\,(j = \sqrt{-1})$ into equation (13) yields the frequency response function matrix of the vibration response

$$[H(j\omega)] = \left[K - M\omega^2 + j\omega C\right]^{-1}[K_t]. \tag{14}$$

2.2. Vehicle Longitudinal and Vertical Vibrations. The frequency response characteristics of the coupled model can be found through equation (14). If the coupling between the front and rear masses of the vehicle is small, the study of vehicle vibration characteristics can be carried out separately for the front and rear suspensions.

The response characteristics of the vehicle vibration can be analyzed using the single wheel model shown in Figure 2.

Figure 2(a) shows the 2-DOF vertical vibration model of the vehicle. m_1 and m_2 are the sprung and unsprung masses, respectively; B_{eqz} and K_{eqz} are the equivalent damping coefficient and equivalent stiffness of the suspension, respectively; K_{tz} is the vertical stiffness of the tyre.

The vibrations of the system can be represented by the displacements of these two masses, so giving two coupled differential equations:

$$\begin{cases} m_1\ddot{Z}_1 + B_{eqz}\left(\dot{Z}_1 - \dot{Z}_2\right) + K_{eqz}\left(Z_1 - Z_2\right) = 0, \\ m_2\ddot{Z}_2 - B_{eqz}\left(\dot{Z}_1 - \dot{Z}_2\right) - K_{eqz}\left(Z_1 - Z_2\right) + K_{tz}\left(Z_2 - Z_3\right) = 0. \end{cases} \tag{15}$$

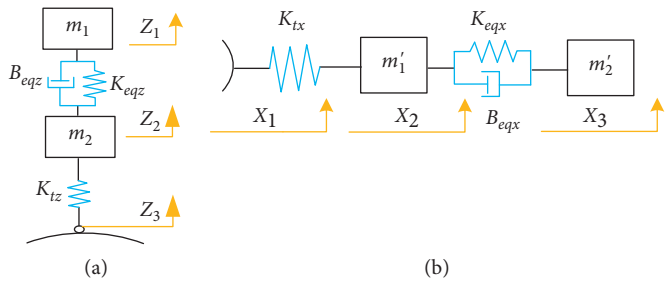

Figure 2: Two-degree-of-freedom two-mass vibration model: (a) vertical; (b) longitudinal.

The frequency response functions of the tyre dynamic load F_d, the suspension dynamic deflection σ_d, and the acceleration $\ddot{Z}_1$ of the suspension vertical vibration response to the road excitation velocity $\ddot{Z}_3$ can be calculated, respectively.

$$\begin{cases} f_{\ddot{Z}_1 \sim \dot{Z}_3} = \dfrac{j\omega r_k + 2r_k\xi\lambda j^2\omega}{\left(1-\lambda^2\right)\left(1+r_k-\lambda^2/r_m\right)-1+\left[r_k-\left(1+r_m/r_m\right)\lambda^2\right]2\xi\lambda j}, \\ f_{\sigma_d \sim \dot{Z}_3} = \dfrac{\left(r_k-\lambda^2 r_k\right)+2\xi\lambda r_k j}{j\omega\left[\left(1-\lambda^2\right)\left(1+r_k-\lambda^2/r_m\right)-1\right]+2j\omega\xi\lambda r_k+\left[\left(1+r_m\right)\lambda^2/r_m\right]\omega}, \\ f_{F_d \sim \dot{Z}_3} = \dfrac{K_{tz}\left(r_k-\lambda^2 r_k\right)+2\xi\lambda r_k j}{j\omega\left[\left(1-\lambda^2\right)\left(1+r_k-\lambda^2/r_m\right)-1\right]-\left[r_k-\left(1+r_m/r_m\right)\lambda^2\right]2\xi\lambda\omega}, \end{cases} \tag{16}$$

where

$$\begin{aligned} r_k &= \frac{K_{tz}}{K_{eqz}}, \\ r_m &= \frac{m_1}{m_2}, \\ \omega_0 &= \sqrt{\frac{K_{eqz}}{m_1}}, \\ \lambda &= \frac{\omega}{\omega_0}, \\ \xi &= \frac{B_{eqz}}{2\sqrt{K_{eqz}m_1}}, \end{aligned} \tag{17}$$

where r_k is the vertical stiffness ratio; ξ is the damping ratio in the vertical direction; r_m is the mass ratio; ω_0 is the vertical natural frequency of the suspension; and λ is the frequency ratio.

Figure 2(b) shows the 2-DOF longitudinal vibration model of the vehicle. K_{tx} is the longitudinal stiffness of the tyre; m_1' is considered to be only the front unsprung mass. The rear unsprung mass can be considered to be fixed to the sprung mass and thus equal to m_2' [5]; K_{eqx} is the equivalent longitudinal stiffness of the suspension. Similar to the vertical vibration, the differential equation of vehicle longitudinal vibration can be expressed as

$$\begin{cases} m_2'\ddot{X}_3 - B_{eqx}\left(\dot{X}_2-\dot{X}_3\right) - K_{eqx}\left(X_2-X_3\right) = 0, \\ m_1'\ddot{X}_2 + B_{eqx}\left(\dot{X}_2-\dot{X}_3\right) + K_{eqx}\left(X_2-X_3\right) = K_{tx}\left(X_1-X_2\right). \end{cases} \tag{18}$$

The frequency response functions of the acceleration $\ddot{X}_3$ to the road excitation velocity $\dot{X}_1$ can be calculated

$$f_{\ddot{X}_3 \sim \dot{X}_1} = \frac{j\omega r_k' - 2rr_k'\xi'\lambda'\omega}{\left(1-\lambda'^2\right)\left(1+r_k'-\lambda'^2/r_m'\right)-1+\left[r_k'-\left(1+r_m'/r_m'\right)\lambda'^2\right]2\xi'\lambda' j}, \tag{19}$$

where

$$\begin{aligned} r_k' &= \frac{K_{tx}}{K_{eqx}}, \\ r_m' &= \frac{m_2'}{m_1'}, \\ \omega_0' &= \sqrt{\frac{K_{eqx}}{m_2'}}, \\ \lambda' &= \frac{\omega'}{\omega_0'}, \\ \xi' &= \frac{B_{eqx}}{2\sqrt{K_{eqx}m_2'}}, \end{aligned} \tag{20}$$

where r_k' is the longitudinal stiffness ratio; ξ' is the longitudinal damping ratio; r_m' is the mass ratio; ω_0' is the longitudinal natural frequency of the suspension; and λ' is the frequency ratio.

From equation (16), the frequency response function of vertical vibration shows that the vertical natural frequency and damping ratio of suspension make an impact on response of the vertical vibration acceleration, the suspension dynamic deflection, and the tyre dynamic load. From equation (19), it can be seen that the longitudinal natural frequency and damping ratio of suspension make an impact on the response of longitudinal vibration acceleration.

From equation (17), it can be seen that the vertical natural frequency and vertical damping ratio of the suspension are influenced by the vertical stiffness of the suspension. From equation (20), it can be seen that the longitudinal natural frequency and longitudinal damping ratio of the suspension are influenced by the longitudinal stiffness of the suspension. From equation (9) it can be seen that the front and rear suspension vibration characteristics make an impact on the pitching behaviour of the vehicle.

Consequently, well-matched suspension stiffness and damping can enhance the vehicle ride comfort. In this study, a full vehicle model with the MacPherson front suspension and the E-type multilink rear suspension is used as an example to analyze the suspension stiffness and to optimize the vibration characteristics.

3. Stiffness Characteristics Analysis of Suspensions

3.1. Stiffness of the Suspension. Neglecting the influence of the bushings and antiroll bar on the suspension stiffness, the suspension stiffness satisfies the following relationship:

$$K_{eq} = K_s i^2, \tag{21}$$

where K_{eq} is the suspension stiffness; K_s is the spring stiffness; and i is the installation ratio.

Taking McPherson suspension as an example, equation (21) is described in detail.

Neglecting the mass of the suspension strut and the control arm, considering the vertical displacement of the vehicle only, the quarter-vehicle model of the MacPherson suspension can be simplified to the model shown in Figure 3 [22]. A is the connection point between the MacPherson suspension strut and the control arm; B is the connection point between the control arm and the body. The global coordinate system is established with the point B as the reference point, Z-axis and Y-axis along with the vertical and horizontal directions, respectively.

In a MacPherson suspension, the position and orientation of the control arm determine the relative movement between the wheel assembly and the chassis. The movement of the system can be seen as a rotational movement around a transient centre O. F_1 is the tangential force acting on the control arm at point A; F_2 is the spring force acting on the control arm at point A; β is the angle between F_1 and F_2; F_4 is the tangential force acting at point C; F_3 is the equivalent spring force acting at the point C; α is the angle between F_3 and F_4; l_{OA} and l_{OC} are the lengths of point A and point C to point R, respectively; Z_1 and Z_2 are the vertical displacements of the wheel and the suspension, respectively.

The following relationships can be obtained:

$$\begin{cases} F_1 = F_2\cos\beta, \\ F_4 = F_3\cos\alpha, \\ F_1 l_{OA} = F_4 l_{OC}, \\ \dfrac{l_{OA}}{l_{OC}} = \dfrac{Z_2\cos\beta}{Z_1\cos\alpha}, \\ F_3 = \dfrac{Z_2}{Z_1}\left(\dfrac{\cos\beta}{\cos\alpha}\right)^2 F_2. \end{cases} \tag{22}$$

In the linear range, the deformation is proportional to the force applied

$$\begin{aligned} F_3 &= K_{eq}Z_1, \\ F_2 &= K_s Z_2. \end{aligned} \tag{23}$$

The linear equivalent stiffness K_{eq} and installation ratio i can be obtained from equations (22) and (23)

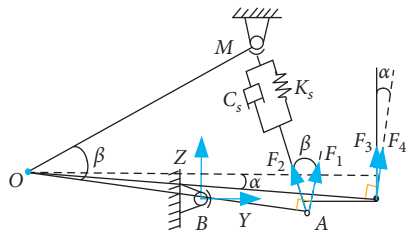

Figure 3: Suspension forces schema for determining equivalent spring force.

$$K_{eq} = \left(\frac{Z_2}{Z_1}\frac{\cos\beta}{\cos\alpha}\right)^2 K_s,$$
$$i = \frac{Z_2}{Z_1}\frac{\cos\beta}{\cos\alpha}. \tag{24}$$

From equation (24), it can be seen that the vertical stiffness K_{eq} of the suspension is influenced by the spring stiffness K_s and the installation ratio i.

For a multilink rear suspension, the vertical stiffness also satisfies equation (21).

The above analysis does not consider the stiffness of the bushings, whereas, for suspension systems, elastic elements such as bushings are installed to absorb impacts. The vertical stiffness of the suspension is influenced by the spring stiffness and bushing stiffness. The deformation of the bushing makes an impact on the installation ratio i. As for the longitudinal stiffness of the suspension, in addition to being influenced by the longitudinal component of the suspension springs and shock absorber, it is mainly influenced by the stiffness of the bushings. Therefore, the suspension will be analyzed specifically with considering the stiffness of the bushings. In the actual driving of a vehicle, the excitation signals transmitted to the bushings are mainly of low-frequency excitation. Therefore, the influence of bushing stiffness on vehicle ride comfort can be studied by considering the static stiffness of the bushing only.

This paper presents the further analysis of the bushings by establishing the static equilibrium equation of the suspension.

3.2. Static Equilibrium Equations for MacPherson Front Suspension. Figure 4 shows the schematic diagram of the MacPherson suspension. The control arm and steering tie rod are connected to the wheel knuckle by ball joint. Control arm is connected to the body by bushings. When an external load is applied to the tyre contact point, the bushings and spring of suspension will deform, and the tie rod will move to a new position, thus achieving a new static equilibrium.

This section will calculate the forces and moments of the bushings with the methods in reference [23].

The relative displacement of the bushing's inner tube to the bushing's outer tube is required. For the bushings of the MacPherson suspension control arm, the displacement of the outer tube can be considered as zero as the outer tube of the bushing is fixed to the body. Therefore, the displacement

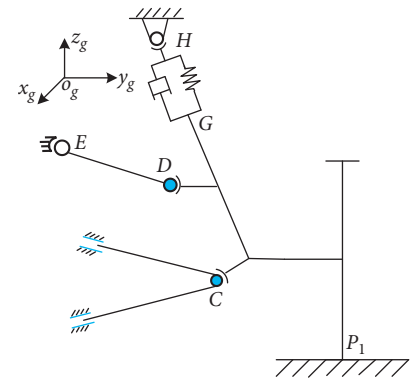

Figure 4: Schematic of MacPherson suspension.

of the inner tube is only required. Firstly, taking point C as a reference point to derive the new coordinates of the inner tube of A and B,

$$\begin{cases} A^* = [X(\alpha)][Y(\beta)][Z(\gamma)]\left(A^0 - C^0\right) + C^*, \\ B^* = [X(\alpha)][Y(\beta)][Z(\gamma)]\left(B^0 - C^0\right) + C^*, \end{cases} \tag{25}$$

where A^*, B^*, and C^* are the new coordinates of the inner tube of bushings A, B, and C in the global coordinate system, respectively; A^0, B^0, and C^0 are the initial coordinates of the inner tube of bushings A, B, and C in the global coordinate system, respectively; $[X(\alpha)]$, $[Y(\beta)]$, and $[Z(\gamma)]$ are the (3×3) rotation matrixes when the control arm is rotated by an angle of α, β, and γ about the x-, y-, and z-axes of its rigid coordinate system, respectively.

The new coordinates of the ball joints D and G, which are connected to the wheel knuckle, and the new coordinates of point P_1 can also be estimated using point C as a reference point.

$$\begin{cases} D^* = [X(\alpha_k)][Y(\beta_k)][Z(\gamma_k)]\left(D^0 - C^0\right) + C^*, \\ G^* = [X(\alpha_k)][Y(\beta_k)][Z(\gamma_k)]\left(G^0 - C^0\right) + C^*, \\ P_1^* = [X(\alpha_k)][Y(\beta_k)][Z(\gamma_k)]\left(P_1^0 - C^0\right) + C^*. \end{cases} \tag{26}$$

where $[X(\alpha_k)]$, $[Y(\beta_k)]$. and $[Z(\gamma_k)]$ are the (3×3) rotation matrixes when the wheel knuckle is rotated by an angle of α_k, β_k, and γ_k about the x-, y-, and z-axes of its rigid coordinate system, respectively.

Thus, the translational deformation of bushing A and bushing B in the global coordinate system r_A' and r_B' is expressed as

$$\begin{bmatrix} r_A' \\ r_B' \end{bmatrix} = \begin{bmatrix} A^* - A^0 \\ B^* - B^0 \end{bmatrix} + \begin{bmatrix} r_A'^0 \\ r_B'^0 \end{bmatrix}, \tag{27}$$

where $r_A'^0$ and $r_A'^0$ are the initial translational displacements of bushings A and B in the global coordinate system.

The forces acting on the bushings due to the displacements of bushings A and B in the global coordinate system can be expressed as

$$\begin{bmatrix} F_A \\ F_B \end{bmatrix} = \begin{bmatrix} K_{A,t} & 0 \\ 0 & K_{B,t} \end{bmatrix} \begin{bmatrix} r_A' \\ r_B' \end{bmatrix} + \begin{bmatrix} \overline{\Delta}_{B,t} \\ \overline{\Delta}_{C,t} \end{bmatrix}, \tag{28}$$

where $\overline{\Delta}_{B,t}$ and $\overline{\Delta}_{C,t}$ are the force-displacement correction vectors of bushing A and bushing B in the global coordinate system, respectively; $K_{A,t}$ and $K_{B,t}$ are the linear stiffness matrixes for bushing A and bushing B in the global coordinate system, respectively.

$K_{A,t}$ can be calculated from the linear stiffness matrix $\overline{K}_{A,t}$ of the bushing A in the local coordinate system. $K_{B,t}$ can be calculated from the linear stiffness matrix $\overline{K}_{B,t}$ of the bushing B in the local coordinate system.

$$\begin{cases} K_{A,t} = R_S^T \overline{K}_{A,t} R_S, \\ K_{B,t} = R_S^T \overline{K}_{B,t} R_S. \end{cases} \tag{29}$$

R_S is the transformation matrix from the local to the global coordinate system of the bushings A and B.

The rotational deformations θ_A' and θ_B' of the bushings A and B in the global coordinate system can be expressed as

$$\begin{bmatrix} \theta_A' \\ \theta_B' \end{bmatrix} = \begin{bmatrix} \theta_A \\ \theta_B \end{bmatrix} + \begin{bmatrix} \theta_A^0 \\ \theta_B^0 \end{bmatrix}, \tag{30}$$

where θ_A and θ_B are rotation angles at load input and θ_A^0 θ_B^0 are rotation initial displacements.

The moments of the bushing A and bushing B in the global coordinate system can be calculated

$$\begin{bmatrix} M_A \\ M_B \end{bmatrix} = \begin{bmatrix} K_{A,r} & 0 \\ 0 & K_{B,r} \end{bmatrix} \begin{bmatrix} \theta_A' \\ \theta_B' \end{bmatrix} + \begin{bmatrix} \overline{\Delta}_{A,r} \\ \overline{\Delta}_{B,r} \end{bmatrix}, \tag{31}$$

where $\overline{\Delta}_{A,r}$ and $\overline{\Delta}_{B,r}$ are the moment-angle correction vectors of bushing A and bushing B in the global coordinate system, respectively; $K_{A,r}$ and $K_{B,r}$ are the linear translational stiffness matrixes of bushing A and bushing B in the global coordinate system, respectively.

$K_{A,r}$ can be calculated from the linear stiffness matrix $\overline{K}_{A,r}$ of the bushing A in the local coordinate system. $K_{B,r}$ can be calculated from the linear stiffness matrix $\overline{K}_{B,r}$ of the bushing B in the local coordinate system.

$$\begin{cases} K_{A,r} = R_S^T \overline{K}_{A,r} R_S, \\ K_{B,r} = R_S^T \overline{K}_{B,r} R_S. \end{cases} \tag{32}$$

According to equations (28) and (31), the reaction forces and moments acting on the control arms of bushing A and bushing B can be derived as follows:

$$\begin{bmatrix} RF_i \\ RM_i \end{bmatrix} = \begin{bmatrix} I & 0 \\ \widetilde{R} & I \end{bmatrix} \begin{bmatrix} -F_i \\ -M_i \end{bmatrix}. \tag{33}$$

Subscript i represents bushings A and B; $[\widetilde{R}]$ is the (3×3) skew-symmetric matrix of the position vector for bushings A and B

$$[\widetilde{R}] = \begin{bmatrix} 0 & z & y \\ z & 0 & -x \\ -y & x & 0 \end{bmatrix}, \tag{34}$$

where x, y, and z represent the displacements of the bushing in the global coordinate system in the directions of the x-, y-, and z-axes, respectively.

The control arm is in equilibrium under the reaction forces, the reaction moments of the bushings, and the ball joints of the wheel knuckle, and therefore the following relationships can be obtained:

$$\begin{cases} RF_A + RF_B + F_C = 0, \\ RM_A + RM_B = 0. \end{cases} \tag{35}$$

The wheel knuckle is in equilibrium under the reaction forces and moments from the control arms, the tie rod, and the external load at the tyre contact patch and therefore satisfies the following relationships:

$$\begin{cases} F_{P1} + RF_C + RF_D + RF_G = 0, \\ M_{P1} + RM_D + RM_G = 0, \end{cases} \tag{36}$$

where M_{P1} is the external force input to the tyre from the road; RF_G and RM_G are the spring reaction force and reaction moment, respectively.

Since the length of the steering tie rod is constant during the suspension kinematics, a constraint can be given

$$L_{ED}' - L_{ED} = 0. \tag{37}$$

The spring deformation satisfies the following constraints:

$$L_{GH}' + \Delta L_{GH} - L_{GH} = 0, \tag{38}$$

where L_{GH}' is the new length of the spring; L_{GH} is the initial length of the spring; and ΔL_{GH} is the displacement of the spring. ΔL_{GH} can be calculated by

$$\Delta L_{GH} = \frac{(f_s L_{ED}' - f_{s0} L_{GH})}{K_s}, \tag{39}$$

where f_{s0} is the initial scale factor of spring force; f_s is the new scale factor of spring force; and K_s is the stiffness of spring.

According to (35)–(38), the static equilibrium equation for the front suspension can be expressed as

$$\begin{Bmatrix} RF_A + RF_B + F_C \\ RM_A + RM_B \\ F_{P1} + RF_C + RF_D + RF_G \\ M_{P1} + RM_D + RM_G \\ L_{ED}' - L_{ED} \\ L_{GH}' + \Delta L_{GH} - L_{GH} \end{Bmatrix} = 0. \tag{40}$$

There are 14 equations in equation (40) and the number of unknowns is 14. Therefore, equation (40) can be solved

3.3. Static Equilibrium Equations for E-Type Multilink Rear Suspensions. Figure 5 shows a diagram of the E-type multilink rear suspension. S_1 is the upper control arm; S_2 is the rear lower control arm; S_3 is the front lower control arm; S_4 is the trailing arm; $B_i\,(i = 1 \sim 3)$ are bushings for the connecting rod to the body; $A_i\,(i = 1 \sim 3)$ are the bushings for connecting the wheel knuckle to the rod; A_4 is the bushing for the trailing arm to the body.

This section will calculate the forces and moments of the bushings with the methods in reference [23, 24].

The new position after the bushing movement was calculated first. Since the outer tube of bushing A_i is connected to the wheel knuckle and the inner tube connected to the rod, both the inner and outer tubes of bushing A_i will move. The displacement of the centre point of both the inner and outer tubes needs to be taken into account. As the outer tubes of bushing B_i and bushing A_4 are fixed to the body, the displacement at the centre of the outer tube will be considered as zero and the displacement at the centre of the inner tube of the bushing will be taken into account.

The centre points of the inner and outer tubes of the bushing coincide at the initial position. $A_i^0\,(i = 1 \sim 3)$ is the coordinate of the centre point of the inner and outer tubes of bushing $A_i\,(i = 1 \sim 3)$ in the global coordinate system at the initial position. B_i^0 is the coordinate of the centre point of the inner and outer tubes of the bushing $B_i\,(i = 1 \sim 3)$ in the global coordinate system at the initial position.

Choose B_i^0 as the reference point and calculate the new coordinates of the centre point of the inner tube A_{li}^* of the bushing A_i in the global coordinate system.

$$A_{li}^* = [X(\alpha_l)][Y(\beta_l)][Z(\gamma_l)]\left(A_i^0 - B_i^0\right) + B_{li}^*, \tag{41}$$

where B_{li}^* is the new coordinate of the centre point of the inner tube of bushing B_i in the global coordinate system; $[X(\alpha_l)]$, $[Y(\beta_l)]$ and $[Z(\gamma_l)]$ are the (3×3) rotation matrixes when the rod is rotated by an angle of α_l, β_l, and γ_l about the x-, y-, and z-axes of its rigid coordinate system, respectively.

Choose P_1 as the reference point and calculate the new coordinates of the centre point of the inner tube A_{l4}^* of bushing A_4 in the global coordinate system.

$$A_{ki}^* = [X(\alpha_k)][Y(\beta_k)][Z(\gamma_k)]\left(A_i^0 - P_1\right) + P_1^*, \tag{42}$$

where P_1^* is the new coordinate of the centre point P_1 in the global coordinate system.

By choosing P_1 as the reference point, the new coordinates of the inner tube A_{l4}^* of the bushing A_4 in the global coordinate system can be calculated

$$A_{l4}^* = [X(\alpha_k)][Y(\beta_k)][Z(\gamma_k)]\left(A_{l4}^0 - P_1\right) + P_1^*, \tag{43}$$

where $[X(\alpha_k)]$, $[Y(\beta_k)]$, and $[Z(\gamma_k)]$ are the (3×3) rotation matrixes when the wheel knuckle is rotated by an angle of α_k, β_k, and γ_k about the x-, y-, and z-axes of its rigid coordinate system, respectively.

The new coordinates of the centre points of the inner and outer tubes of the bushing can be calculated by equations (41)–(43).

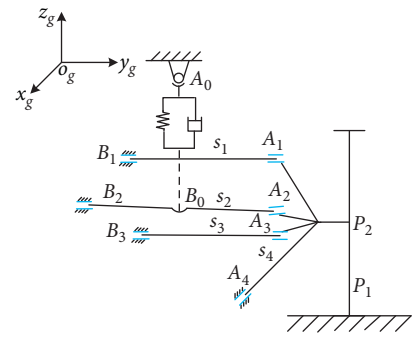

Figure 5: Schematic of MacPherson suspension.

Based on the preceding analysis, the translational and rotational deformations of bushing B_i in the global coordinate system can be expressed as

$$\begin{bmatrix} r_{B_i}' \\ \theta_B' \end{bmatrix} = \begin{bmatrix} B_{li}^* - B_i^0 \\ \theta_{B_{li}} \end{bmatrix} + \begin{bmatrix} r_{B_i}'^0 \\ \theta_{B_i}'^0 \end{bmatrix}, \tag{44}$$

where $\theta_{B_{li}}$ is the rotational angle of bushing B_i in the global coordinate system under the force of the rod; $r_{B_i}'^0$ and $\theta_{B_i}'^0$ are the initial translational displacements and the initial rotational angles of bushing B_i.

The forces and moments applied to bushing B_i in the global coordinate system can be expressed as

$$\begin{bmatrix} F_{B_{li}} \\ M_{B_{li}} \end{bmatrix} = \begin{bmatrix} K_{B_i,t} & 0 \\ 0 & K_{B_i,r} \end{bmatrix} \begin{bmatrix} r_{Bi}' \\ \theta_{Bi}' \end{bmatrix} + \begin{bmatrix} \overline{\Delta}_{B_i,t} \\ \overline{\Delta}_{B_i,r} \end{bmatrix}, \tag{45}$$

where $\overline{\Delta}_{B_i,t}$ and $\overline{\Delta}_{B_i,r}$ are the moment-angle and the force-displacement correction vectors for bushing B_i in the global coordinate system, respectively; $K_{B_i,t}$ and $K_{B_i,r}$ are the linear translational stiffness matrixes for bushing B_i in the global coordinate system, respectively.

$K_{B_i,t}$ and $K_{B_i,r}$ can be calculated from the linear stiffness matrices $\overline{K}_{B_i,t}$, $\overline{K}_{B_i,r}$ of bushing B_i in the local coordinate system.

$$\begin{cases} K_{B_i,t} = R_S'^T \overline{K}_{B_i,t} R_S', \\ K_{B_i,r} = R_S'^T \overline{K}_{B_i,r} R_S'. \end{cases} \tag{46}$$

R_S' is the (3×3) transformation matrix from the global coordinate system to the local coordinate system of bushing B_i.

The reaction forces $RF_{B_{li}}$ and moments $RM_{B_{li}}$ applied to the rod by bushing B_i in the global coordinate system are therefore

$$\begin{bmatrix} RF_{B_{li}} \\ RM_{B_{li}} \end{bmatrix} = -\begin{bmatrix} F_{B_{li}} \\ M_{B_{li}} \end{bmatrix} = \begin{bmatrix} -K_{B_i,t} & 0 \\ 0 & -K_{B_i,r} \end{bmatrix} \begin{bmatrix} r_{B_i}' \\ \theta_{B_i}' \end{bmatrix} - \begin{bmatrix} \overline{\Delta}_{B_i,t} \\ \overline{\Delta}_{B_i,r} \end{bmatrix}. \tag{47}$$

The deformation of bushing $A_i\,(i = 1 \sim 3)$ satisfies the following relationships:

$$\begin{bmatrix} r'_{A_i} \\ \theta'_{A_i} \end{bmatrix} = \begin{bmatrix} A^*_{li} - A^0_i \\ \theta_{lA_i} \end{bmatrix} - \begin{bmatrix} A^*_{ki} - A^0_i \\ \theta_{kA_i} \end{bmatrix} + \begin{bmatrix} r'^0_{A_i} \\ \theta'^0_{A_i} \end{bmatrix}, \tag{48}$$

where θ_{lA_i} and θ_{kA_i} are the rotational angles in relative to the rod and in relative to the wheel knuckle of the bushing A_i in the global coordinate system when the load is applied, respectively; $r'^0_{A_i}$ and $\theta'^0_{A_i}$ are the initial translational displacements and the initial rotational angles of bushing A_i.

Thus, the forces and moments applied to the inner tube of bushing A_i by the rod in the global coordinate system can be calculated

$$\begin{bmatrix} F_{A_{li}} \\ M_{A_{li}} \end{bmatrix} = \begin{bmatrix} K_{A_i,t} & 0 \\ 0 & K_{A_i,r} \end{bmatrix} \begin{bmatrix} r'_{A_i} \\ \theta'_{A_i} \end{bmatrix} + \begin{bmatrix} \overline{\Delta}_{A_i,t} \\ \overline{\Delta}_{A_i,r} \end{bmatrix}, \tag{49}$$

where $\overline{\Delta}_{A_i,t}$ and $\overline{\Delta}_{A_i,r}$ are the moment-angle and the force-displacement correction vectors for bushing A_i in the global coordinate system, respectively; $K_{A_i,t}$ and $K_{A_i,r}$ are the linear translational stiffness matrix and rotational stiffness matrix of bushing A_i in the global coordinate system, respectively.

$K_{A_i,t}$ and $K_{A_i,r}$ can be calculated from the linear stiffness matrices $\overline{K}_{A_i,t}$, $\overline{K}_{A_i,r}$ of the bushing A_i in the local coordinate system.

$$\begin{cases} K_{A_i,t} = R''^T_s \overline{K}_{A_i,t} R''_s, \\ K_{A_i,r} = R''^T_s \overline{K}_{A_i,r} R''_s, \end{cases} \tag{50}$$

where R''_s is the (3×3) transformation matrix from the global coordinate system to the local coordinate system of bushing A_i.

Combined with equation (49), the reaction force and reaction moment applied to the rod by the inner tube of bushing A_i can be expressed as

$$\begin{bmatrix} RF_{A_{li}} \\ RM_{A_{li}} \end{bmatrix} = \begin{bmatrix} I & 0 \\ \widetilde{R}_{A_i} & I \end{bmatrix} \begin{bmatrix} -F_{A_{li}} \\ -M_{A_{li}} \end{bmatrix}, \tag{51}$$

where I is the (3×3) unity matrix; $\widetilde{R}_{A_i}$ is the (3×3) skew-symmetric matrix of the position vector in the global coordinate system for inner tube of bushing A_i changing with the rods.

Substituting (49) into (51) gives

$$\begin{bmatrix} RF_{A_{li}} \\ RM_{A_{li}} \end{bmatrix} = \begin{bmatrix} -K_{A_i,t} & 0 \\ -\widetilde{R}_{A_i} K_{A_i,t} & -K_{A_i,r} \end{bmatrix} \begin{bmatrix} r'_{A_i} \\ \theta'_{A_i} \end{bmatrix} - \begin{bmatrix} \overline{\Delta}_{A_i,t} \\ \widetilde{R}_{A_i} \overline{\Delta}_{A_i,t} + \overline{\Delta}_{A_i,r} \end{bmatrix},$$

$$\widetilde{R}_{A_i} = \begin{bmatrix} 0 & z' & y' \\ z' & 0 & -x' \\ -y' & x' & 0 \end{bmatrix}, \tag{52}$$

where x', y', and z' are the values of the x, y, and z directions of the position vector for the inner tube of bushing A_i with the rod, respectively.

Since the inner tube of bushing A_i is loaded against the outer tube, the forces and moments applying to the outer tube of the bushing A_i from the wheel knuckle are

$$\begin{bmatrix} F_{A_{ki}} \\ M_{A_{ki}} \end{bmatrix} = -\begin{bmatrix} F_{A_{li}} \\ M_{A_{li}} \end{bmatrix}. \tag{53}$$

Taking the moments at P_1 and combining with equations (49) and (53), the reaction force and moment applied by the bushing A_i to the wheel knuckle can be derived.

$$\begin{bmatrix} RF_{A_{ki}} \\ RM_{A_{ki}} \end{bmatrix} = \begin{bmatrix} I & 0 \\ \widetilde{R}'_{A_i} & I \end{bmatrix} \begin{bmatrix} -F_{A_{ki}} \\ -M_{A_{ki}} \end{bmatrix}, \tag{54}$$

where I is the (3×3) unity matrix; $\widetilde{R}_{Ai}$ is the (3×3) skew-symmetric matrix of the position vector in the global coordinate system for the inner tube of bushing A_i changing with the wheel knuckle.

$$\widetilde{R}'_{A_i} = \begin{bmatrix} 0 & z'_1 & y'_1 \\ z'_1 & 0 & -x'_1 \\ -y'_1 & x'_1 & 0 \end{bmatrix}. \tag{55}$$

Combining equations (49) and (53), equation (54) can be written as

$$\begin{bmatrix} RF_{A_{ki}} \\ RM_{A_{ki}} \end{bmatrix} = \begin{bmatrix} K_{A_i,t} & 0 \\ \widetilde{R}'_{A_i} K_{A_i,t} & K_{B_i,r} \end{bmatrix} \begin{bmatrix} r'_{A_i} \\ \theta'_{A_i} \end{bmatrix} + \begin{bmatrix} \overline{\Delta}_{A_i,t} \\ \widetilde{R}'_{A_i} \overline{\Delta}_{A_i,t} + \overline{\Delta}_{A_i,r} \end{bmatrix}. \tag{56}$$

Similarly, the translational and rotational deformations of bushing A_4 in the global coordinate system can be expressed as

$$\begin{bmatrix} r'_{A_4} \\ \theta'_{A_4} \end{bmatrix} = \begin{bmatrix} A^*_{l4} - A^0_4 \\ \theta_{A_{l4}} \end{bmatrix} + \begin{bmatrix} r'^0_{A_4} \\ \theta'^0_{A_4} \end{bmatrix}, \tag{57}$$

where $\theta_{A_{l4}}$ is the rotational angle of the bushing A_4 in relative to the rod in the global coordinate system when the load is applied; $r'^0_{A_4}$ and $\theta'^0_{A_4}$ are the initial translational displacements and the initial rotational angles of bushing A_i in the global coordinate.

Similarly, the forces and moments applied by the rod on the inner tube of bushing A_4 can be derived. Taking the moments at P_1, the reaction force and moment applied by the bushing A_4 to the wheel knuckle can be derived.

$$\begin{bmatrix} RF_{A_{l4}} \\ RM_{A_{l4}} \end{bmatrix} = \begin{bmatrix} I & 0 \\ \widetilde{R}_{A_4}{}' & I \end{bmatrix} \begin{bmatrix} -F_{A_{l4}} \\ -M_{A_{l4}} \end{bmatrix}, \tag{58}$$

where $\widetilde{R}'_{A_4}$ is the (3×3) skew-symmetric matrix of the position vector in the global coordinate system for the inner tube of bushing A_4 changing with the wheel knuckle.

Consequently, the sum of each reaction force RF, reaction moment RM, and external force applied to the wheel knuckle have a value of zero in the global coordinate system. The static equilibrium equation for the wheel knuckle can be expressed as

$$\begin{cases} F_{P_1} + \sum_{i=1}^{3} RF_{A_{ki}} + RF_{A_{l4}} = 0, \\ \sum_{i=1}^{3} RM_{A_{ki}} + RM_{A_{l4}} = 0, \end{cases} \tag{59}$$

where F_{P1} is the external force applied to the point P_1 on the wheel.

Rod $S_i\,(i = 1, 3)$ is in equilibrium under the reaction forces and moments from the bushings A_i and $B_i\,(i = 1, 3)$. Thus, the static equilibrium equation for the rod S_i $(i = 1, 3)$ can be derived as

$$\begin{cases} RF_{A_{li}} + RF_{B_{li}} = 0, \\ RM_{A_{li}} + RM_{B_{li}} = 0. \end{cases} \tag{60}$$

The lower rear control arm S_2 is connected to the body by the spring. The ends of S_2 are connected to the wheel knuckle and the body by bushings A_2 and B_2. The equations for the static equilibrium of the lower rear control arm S_2 can be derived as

$$\begin{cases} RF_{B_{l2}} + RF_{A_{l2}} + F_{A_0} = 0, \\ RM_{A_{l2}} + RM_{B_{l2}} + M_{A_0} = 0. \end{cases} \tag{61}$$

F_{A_0} and M_{A_0} are the forces and moments applied by the spring with B_2 as the reference point. The initial length, the length after deformation, and the displacement of the spring satisfy the following equation:

$$L'_{A_0B_0} + \Delta L_{A_0B_0} - L_{A_0B_0} = 0, \tag{62}$$

where $L'_{A_0B_0}$ is the length of the spring after deformation; $L_{A_0B_0}$ is the initial length of the spring; and $\Delta L_{A_0B_0}$ is the displacement of the spring. $\Delta L_{A_0B_0}$ can be calculated from

$$\Delta L_{A_0B_0} = \frac{\left(f_s L^*_{A_0B_0} - f_{s0} L_{A_0B_0}\right)}{K_s}, \tag{63}$$

where f_{s0} is the initial scale factor of spring force; K_s is the stiffness of spring.

According to (58)–(61), the static equilibrium equation of the E-type multilink rear suspension can be derived

$$\left\{ \begin{array}{l} \left\{ \begin{array}{l} F_{P_1} + \sum_{i=1}^{3} RF_{A_{ki}} + RF_{A_{l4}} \sum_{i=1}^{3} RM_{A_{ki}} + RM_{A_{l4}} \\ \quad \left\{ \begin{array}{ll} RF_{A_{li}} + RF_{B_{li}} & \\ RM_{A_{li}} + RM_{B_{li}} & (i = 1, 3) \\ RF_{B_{l2}} + RF_{A_{l2}} + F_{A_0} & \\ RM_{A_{l2}} + RM_{B_{l2}} + M_{A_0} & \end{array} \right. \\ L'_{A_0B_0} + \Delta L_{A_0B_0} - L_{A_0B_0} \end{array} \right\} = 0. \end{array} \right. \tag{64}$$

3.4. Bushing Stiffness and Suspension Stiffness. Longitudinal and vertical forces with intervals of [0, 1500] are applied to the front and rear wheel centre, respectively.

The forces of bushing B and bushing A_4 are shown in Figure 6. Taking the example of bushing A, F_A^X represents the force of bushing A in the X direction.

Due to the different stiffness of the bushings, the bushings generate different displacements. Figure 7 shows the displacements of bushing B and bushing A_4. D_A^X represents the displacement of bushing A in the X direction.

As can be seen in Figure 7, the bushings have initial forces and initial displacements in the initial position. Therefore, the values of the change in forces and displacements are used to analyze the influence on bushings. The relevant results are obtained, as shown in Figures 8 and 9.

Bushings A and B are the bushings of front suspension. Bushings $A_i\,(i = 1 \sim 4)$ and $B_i\,(i = 1 \sim 4)$ are the bushings of rear suspension.

As can be seen from Figure 8(a), when longitudinal forces are applied, $F_A^Y, F_{A2}^X, F_{A2}^X, F_{B2}^X, F_{A3}^X, F_{B2}^X$ are more variable. As can be seen from Figure 8(b), when vertical forces are applied, the forces on the front suspension bushings have little variation, while the forces on the rear suspension bushings $F_{A1}^X, F_{B1}^X, F_{A2}^X, F_{B2}^X, F_{A3}^X, F_{B3}^X$ have larger variations.

As can be seen in Figure 9(a), when applying longitudinal forces, D_B^Y and D_{A4}^X are more variable. As can be seen in Figure 9(b), displacements of bushings on the front suspension are minor when the vertical force is applied. For the rear suspension, D_{B3}^Z and D_{A4}^Z are more variable.

The displacements of the bushings will influence the displacement of the wheel centre. Based on the preceding analysis, varying the stiffness of bushing B in the Y direction, the stiffness of bushing A_4 in the X direction and Z direction, and the stiffness of bushing B_3 in the Z direction, the longitudinal displacement vs. longitudinal force curve of wheel centre and the vertical displacement vs. vertical force curve of wheel centre can be obtained, as shown in Figure 10. As can be seen in Figure 10, the force vs. displacement curve changes significantly when changing the stiffness of the mentioned bushings.

The vertical stiffness of suspension can be expressed by the ratio of the vertical load to the vertical displacement of the wheel centre. Longitudinal stiffness is usually defined as the ratio of the longitudinal force to the longitudinal displacement of the wheel centre [5]. The slope of the curve in the linear range, i.e., the linear stiffness of the suspension, can be thus obtained, as shown in Tables 1 and 2.

The stiffness of bushing B in the Y direction is denoted as T_B^Y. The stiffness of bushing A_4 in the X direction is denoted as T_{A4}^X. The stiffness of bushing A_4 in the Z direction is denoted as T_{A4}^Z. The stiffness of bushing B_3 in the Z direction is denoted as T_{B3}^Z.

Table 1 shows the longitudinal stiffness of the front suspension for different stiffness T_B^Y. As seen in Table 1, reducing the stiffness T_B^Y by 50% reduces the longitudinal stiffness of the front suspension by 44.1%, thus showing that the stiffness T_B^Y contributes more than 50% to the longitudinal stiffness of the front suspension. Table 2 shows the longitudinal and vertical stiffness of the rear suspension for different stiffnesses of bushing. As seen in Table 2, reducing the stiffness T_{A4}^X by 50% reduces the longitudinal stiffness of the rear suspension by 41.1%, so the contribution of the stiffness T_{A4}^X to the longitudinal stiffness of the rear suspension is greater than 50%. Reducing the stiffness T_{B3}^Z and

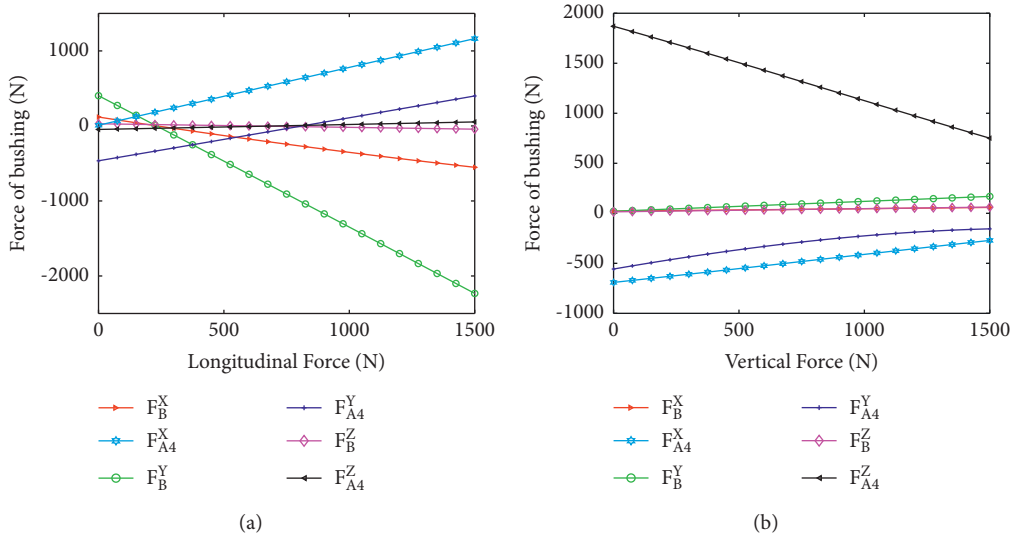

Figure 6: The forces of bushing: applying longitudinal force (a); applying vertical force (b).

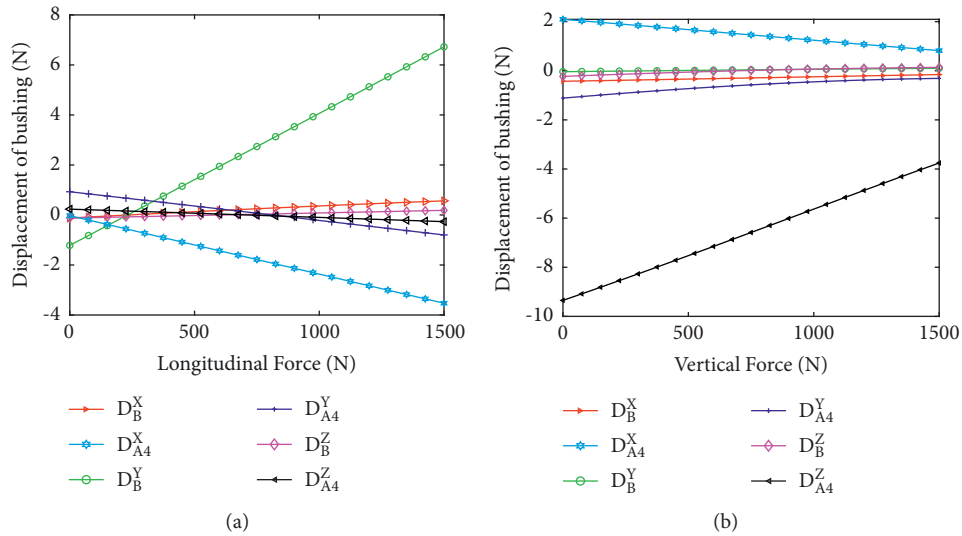

Figure 7: The displacements of bushing: applying longitudinal force (a); applying vertical force (b).

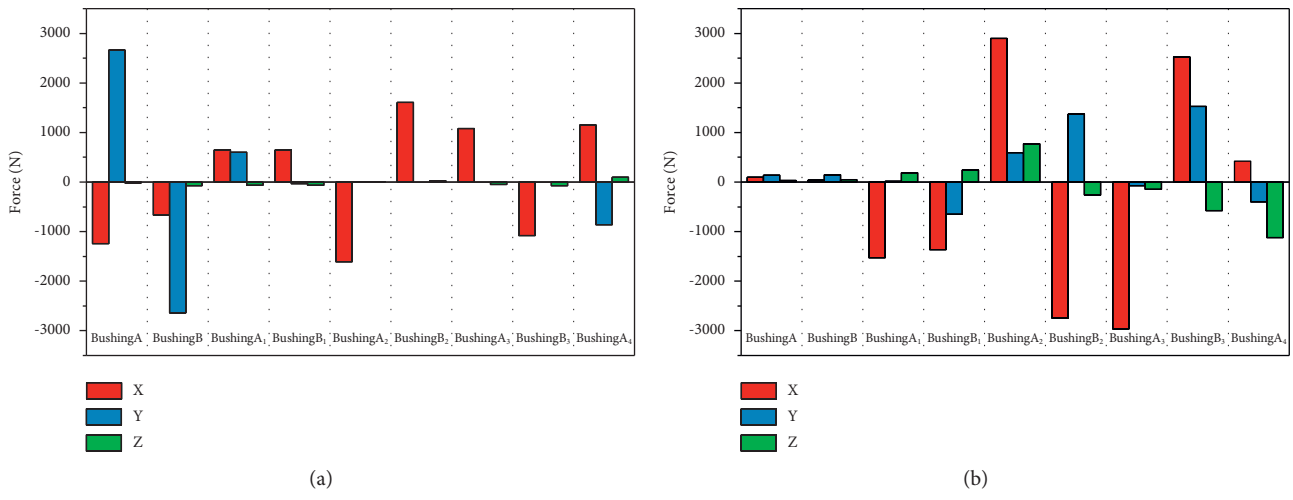

Figure 8: Variation of bushing forces: applying longitudinal force (a); applying vertical force (b).

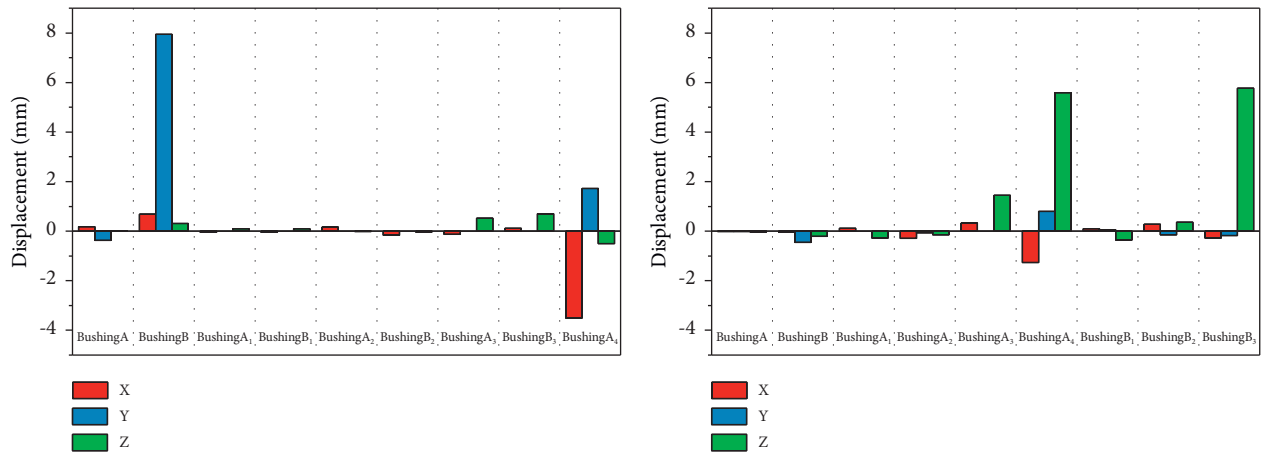

Figure 9: Variation of bushing displacements: applying longitudinal force (a); applying vertical force (b).

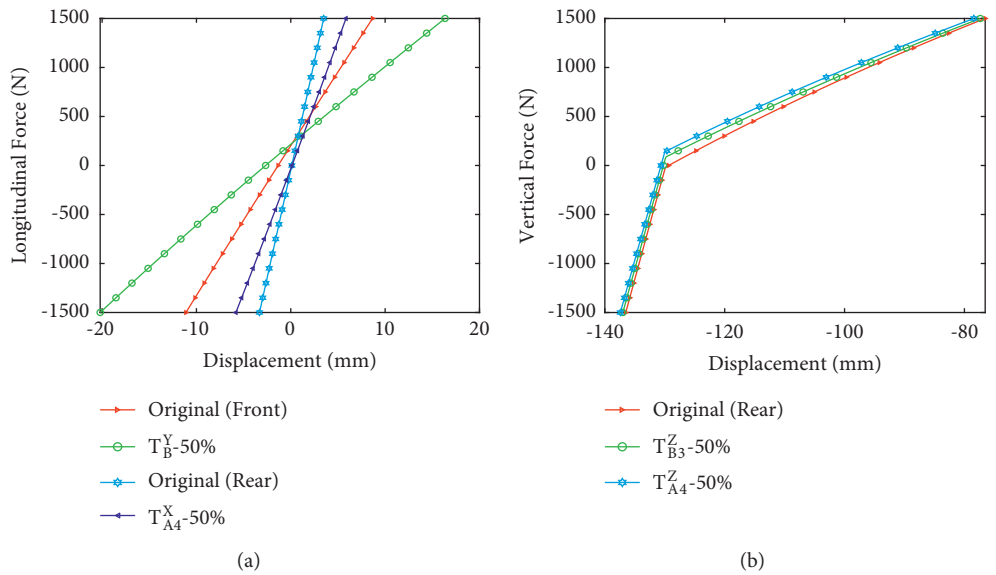

Figure 10: Force vs. displacement curves for suspensions with different stiffnesses of bushing: longitudinal (a); vertical (b).

Table 1: Stiffness of front suspension.

Case	Bush stiffness	Longitudinal stiffness
Baseline (N/mm)	T_B^Y	152
T_B^Y – 50% (N/mm)	166	85

Table 2: Stiffness of rear suspension.

Case	Stiffness	Longitudinal stiffness	Vertical stiffness
Baseline (N/mm)	$T_{A4}^X = 330, T_{B3}^Z = 100,$ $T_{A4}^Z = 200$	443.79	24.67
T_{A4}^X – 50% (N/mm)	165	261.32	—
T_{B3}^Z – 50% (N/mm)	50	—	24
T_{A4}^Z – 50% (N/mm)	100	—	23.29

T_{A4}^{Z} by 50% reduces the rear suspension vertical stiffness by 2.8% and 5.6%, respectively, so it can be seen that the stiffness of these two bushings contributes little to the vertical stiffness of the rear suspension.

From the analysis in Sections 2 and 3, it is clear that the stiffness of the bushings will influence the vibration characteristics of the vehicle.

This paper will analyze the vehicle ride comfort on bump road through simulation study.

4. Analysis of Vehicle Ride Comfort on Bump Road

Simulation study on bump road: the parameters of the simulated vehicle are shown in Table 3, with a bump height of 25 mm and a width of 100 mm. The vehicle will generate vertical and longitudinal vibrations when passing the bump road. As can be seen in Figure 11, the reaction force of the bump road on the tyre can be simplified to the force through the wheel centre F_T and a moment around the wheel centre M_T. M_T will be balanced by the reaction moment generated from the changing of the kingpin caster angle. F_T can be divided into the component force F_1 perpendicular to the line and the component force F_2 acting along the line between the centre of longitudinal inclination O and the wheel centre. F_1 makes the tyres to move upwards, resulting in vertical vibrations. F_2 makes the tyres to move backwards, resulting in longitudinal vibrations.

Using the continuous RMS method, the transient vibrations are taken into account by integrating over short periods of time.

This paper calculates longitudinal and vertical acceleration RMS curves with two different calculation windows.

$$\begin{cases} \text{Rms Local} = \left[\dfrac{1}{\text{Mloc}} \displaystyle\int_{t_0}^{t_0+Mloc} a_w^2(t)\mathrm{d}t\right]^{1/2}, \\ \text{Rms Global} = \left[\dfrac{1}{\text{MGlo}} \displaystyle\int_{t_0}^{t_0+MGlo} a_w^2(t)\mathrm{d}t\right]^{1/2}, \\ \text{Mloc} = 0.52 \times 3.6\dfrac{l}{v} = \dfrac{1.872l}{v}, \\ \text{MGlo} = 1.05 \times 3.6\dfrac{l}{v} = \dfrac{3.78l}{v}, \end{cases} \tag{65}$$

where l is the wheelbase of the vehicle.

Rms Local is the RMS curve of longitudinal and vertical accelerations calculated using a narrow calculation window, which is used to separate the influence of the impact of the front and the rear wheels. Rms Global is the RMS curve of longitudinal and vertical accelerations calculated using a large calculation window, which is used to consider the influence of the impact due to all wheels.

ΔRms Local is the maximum difference between Rms Local during bump passing and before the bump passing. ΔRms Global is the maximum difference between Rms Global during bump passing and before the bump passing. ΔRms Global and ΔRms Global are used to study the transient signals.

Table 3: Vehicle's parameters.

Parameter	Value	Parameter	Value
m (kg)	1815.25	a (mm)	1352.6
l (mm)	2620.0	b (mm)	1247.4
T_B^Y (N/mm)	332	T_{A4}^X (N/mm)	330
K_{sf} (N/mm)	21	K_{sr} (N/mm)	26
B_{sf} (N·s/mm)	1.44	B_{sr} (N·s/mm)	0.976

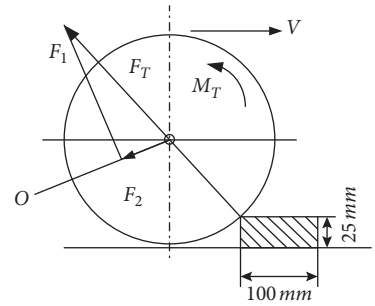

Figure 11: Bump event.

Figure 12 shows the curves of the longitudinal and vertical acceleration time-domain signal, local variation Rms Local, and global variation Rms Global of the front and rear seat rails when the vehicle passes over the bump road at the speed of 30 km/h.

As can be seen in Figure 12, the curve of local variation Rms Local has two significant peaks due to the influence of the front and rear wheels. The value of ΔRms Local is greater than ΔRms Global.

Longitudinal ΔRms Local and longitudinal ΔRms Global of the front seat rail are greater than the rear suspension. The vertical ΔRmsLocal and vertical ΔRmsGlobal of the rear seat rail are greater than the front suspension.

The influence of the front and rear suspension parameters on the ΔRmsLocal and ΔRmsGlobal of the front and rear seat rails was analyzed by sensitivity. The top 10 parameters with high impact are shown in Figure 13.

As can be seen in Figure 13, the stiffness T_B^Y of the bushing B has a significant influence on the longitudinal ΔRmsLocal and ΔRmsGlobal of the front seat rail. The stiffness of the spring and the damping of the shock absorber of the front suspension have a greater influence on the vertical ΔRmsLocal and ΔRmsGlobal of the front seat rail. The stiffness T_{A4}^X of bushing A_4 has a significant influence on the longitudinal ΔRmsLocal and ΔRmsGlobal of the rear seat rail. The stiffness of the spring and the damping of the shock absorber of the rear suspension have a greater influence on the vertical ΔRmsLocal and ΔRmsGlobal of the rear seat rail.

From the analysis of the suspension stiffness characteristics in Section 3, it is clear that the longitudinal stiffness of the front suspension is influenced by the stiffness T_B^Y of bushing B mostly and the longitudinal stiffness of the rear suspension is influenced by the stiffness T_{A4}^X of bushing A_4

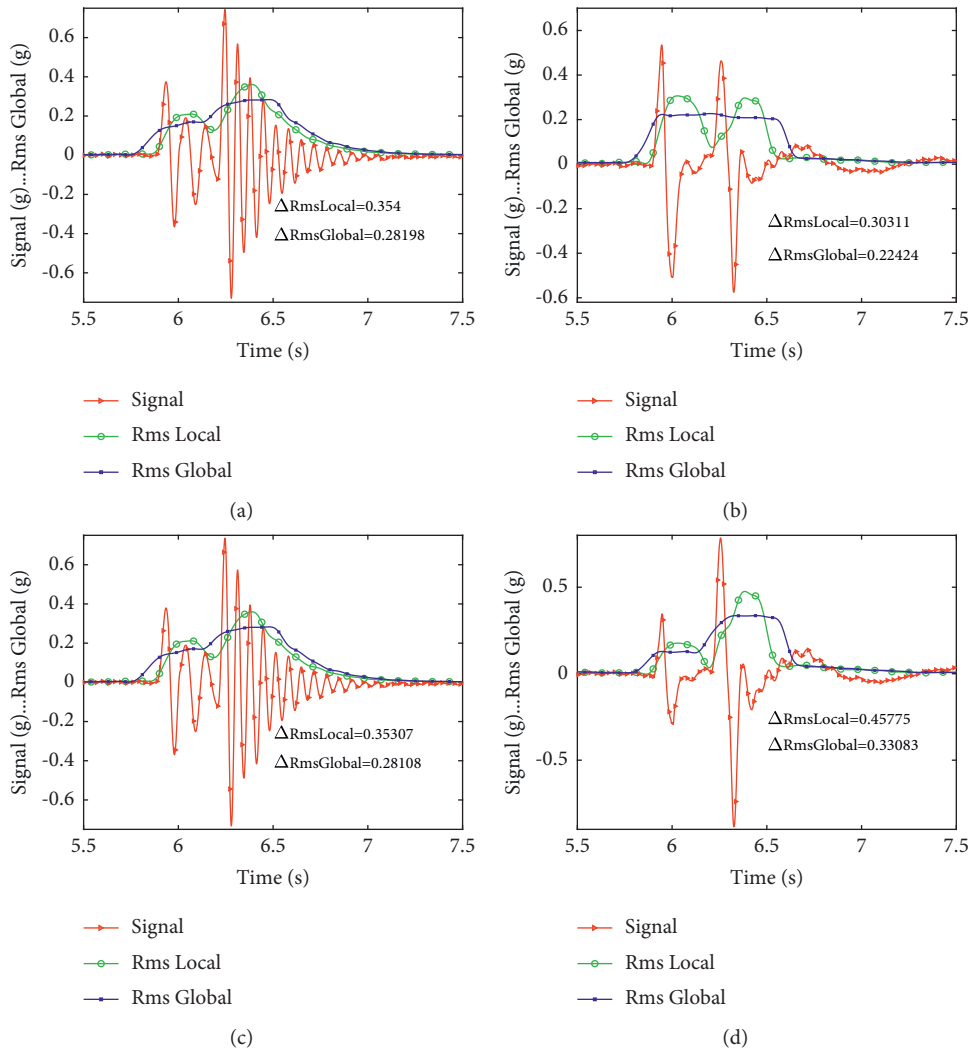

FIGURE 12: Signal and indexes: front seat rail in the longitudinal direction (a); front seat rail in the vertical direction (b); rear seat rail in the longitudinal direction (c); rear seat rail in the vertical direction (d).

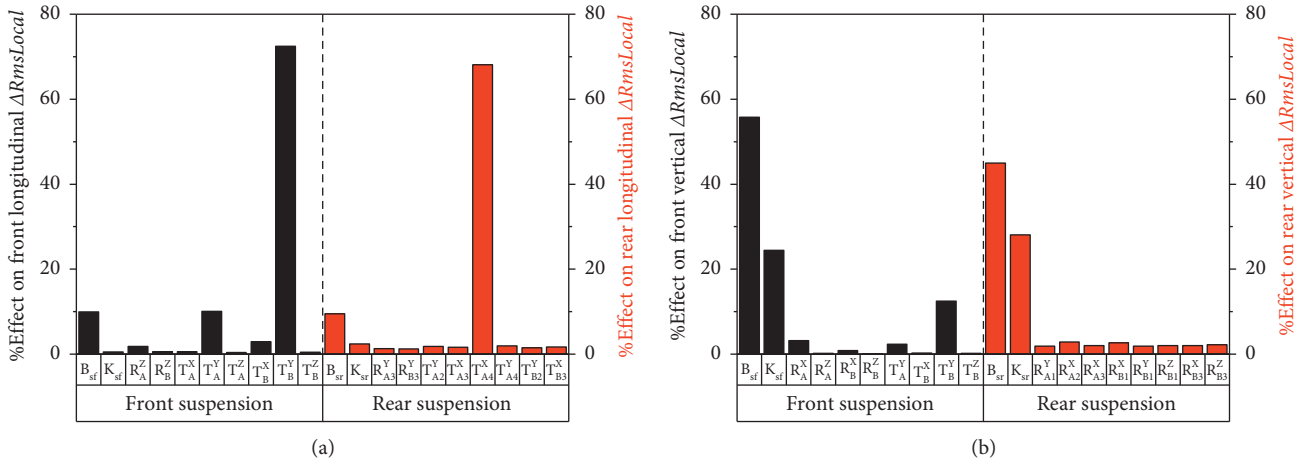

FIGURE 13: Continued.

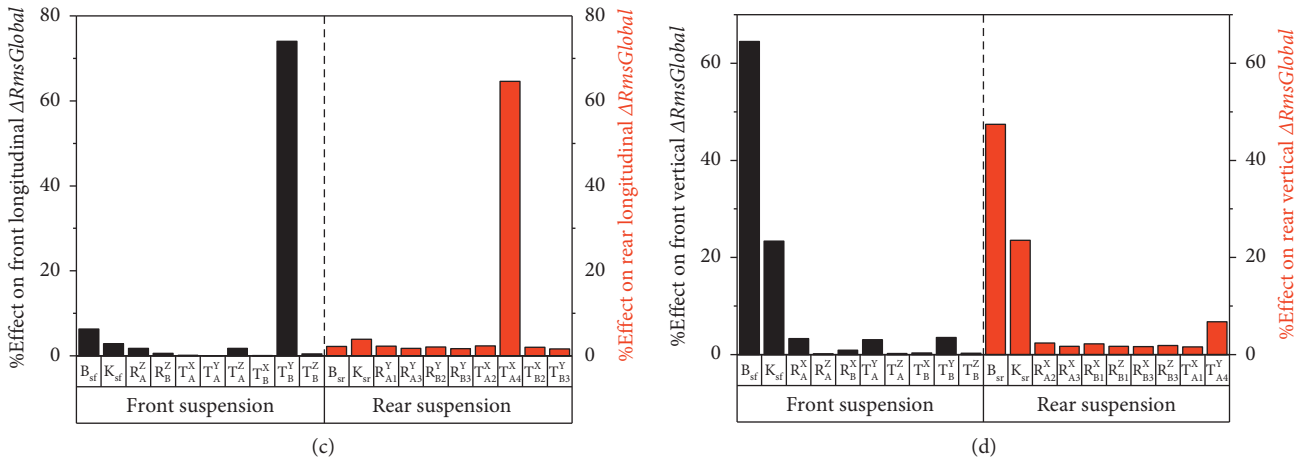

FIGURE 13: The effect of suspension parameters on the indexes: longitudinal ΔRmsLocal (a); vertical ΔRmsLocal (b); longitudinal ΔRmsGlobal (c); vertical ΔRmsGlobal (d).

mostly, while the bushing stiffness has little influence on the vertical stiffness of suspension. Combined with (28), it can be seen that the vertical stiffness of suspension is influenced by the spring stiffness mostly.

From the analysis of the vehicle vibration characteristics in Section 2, it can be seen that the natural frequency and damping ratio of the suspension influence the acceleration relative to the road excitation response. The natural frequency of the suspension is influenced by the stiffness of suspension. The damping ratio of the suspension is influenced by the stiffness of spring and the damping of the shock absorber. Therefore, the results obtained in Figure 13 are consistent with the previous derivation.

The trends of longitudinal ΔRmsLocal and ΔRmsGlobal of the front and rear seat rails with bushing stiffness are shown in Figure 14. Figures 14(a) and 14(b) show the trends of longitudinal ΔRmsLocal and ΔRmsGlobal of the front seat rail with bushing stiffness T_B^Y at different vehicle speeds. As can be seen from both graphs, the variation of ΔRmsLocal and ΔRmsGlobal with the bushing stiffness T_B^Y is not a linear relationship. The values of longitudinal ΔRmsLocal and ΔRmsGlobal are different for the same vehicle speed with different bushing stiffness T_B^Y. On the other hand, for the same bushing stiffness T_B^Y,the values of longitudinal ΔRmsLocal and ΔRmsGlobal are different for different vehicle speeds. Figures 14(c) and 14(d) show the trends of longitudinal ΔRmsLocal and ΔRmsGlobal of the rear seat rail with the bushing stiffness T_{A4}^X at different vehicle speeds. As can be seen from the two graphs, both ΔRmsGlobal and ΔRmsLocal of the rear seat rail do not have a linear relationship with the bushing stiffness T_{A4}^X. The values of ΔRmsLocal and ΔRmsGlobal of the rear seat rail are also influenced by the bushing stiffness T_{A4}^X and the speed of the vehicle.

5. Optimal Design of Vehicle Ride Comfort

5.1. Multiobjective Optimization Mathematical Model. It is clear from Section 2 that the safety of the vehicle needs to be guaranteed while improving the vehicle ride comfort. As a result, the dynamic deflection of suspensions σ_{df} and σ_{dr} needs to be used as a constraint. The spring stiffnesses K_{sf} and K_{sr} of the front and rear suspension, the damping coefficients B_{sf} and B_{sr} of the front and rear shock absorbers, the stiffness of the bushing T_B^Y for the front suspension, and the stiffness of the bushing T_{A4}^X of the rear suspension are therefore used as optimization variables. From the analysis of Figure 14, it can be seen that the stiffness of the bushings that make ΔRmsLocal and ΔRmsGlobal lower are approximately the same, and the value of ΔRmsLocal is greater than the value of ΔRmsGlobal. To reduce the amount of calculation, this paper takes the ΔRmsLocal of the front and rear seat rails in the longitudinal and vertical directions as optimization objective 1, the RMS of the dynamic loads $\sigma_{Fdf}, \sigma_{Fdr}$ of the front and rear suspensions as optimization objective 2, and the RMS of pitch angle acceleration σ_p for the body as optimization objective 3. The equation of multiobjective optimization mathematical model can be expressed as

$$\begin{cases} \text{minimize} : \Delta\text{Rms}\, L1, \Delta\text{Rms}\, L2, \Delta\text{Rms}\, L3, \Delta\text{Rms}\, L4, \\ \text{minimize} : \sigma_{Fdf}, \sigma_{Fdr}, \\ \text{minimize} : \sigma_p, \\ \text{subject to} : \sigma_{df} \le \dfrac{1}{3}\left[f_{df}\right], \sigma_{dr} \le \dfrac{1}{3}\left[f_{dr}\right], \\ \text{subject to} : 18.9 \le K_{sf} \le 23.1, 1.296 \le B_{sf} \le 1.584, \\ \text{subject to} : 23.4 \le K_{sr} \le 28.6, 0.878 \le B_{sr} \le 1.074, \\ \text{subject to} : 166 \le T_B^Y \le 498, 165 \le T_{A4}^X \le 495, \end{cases} \tag{66}$$

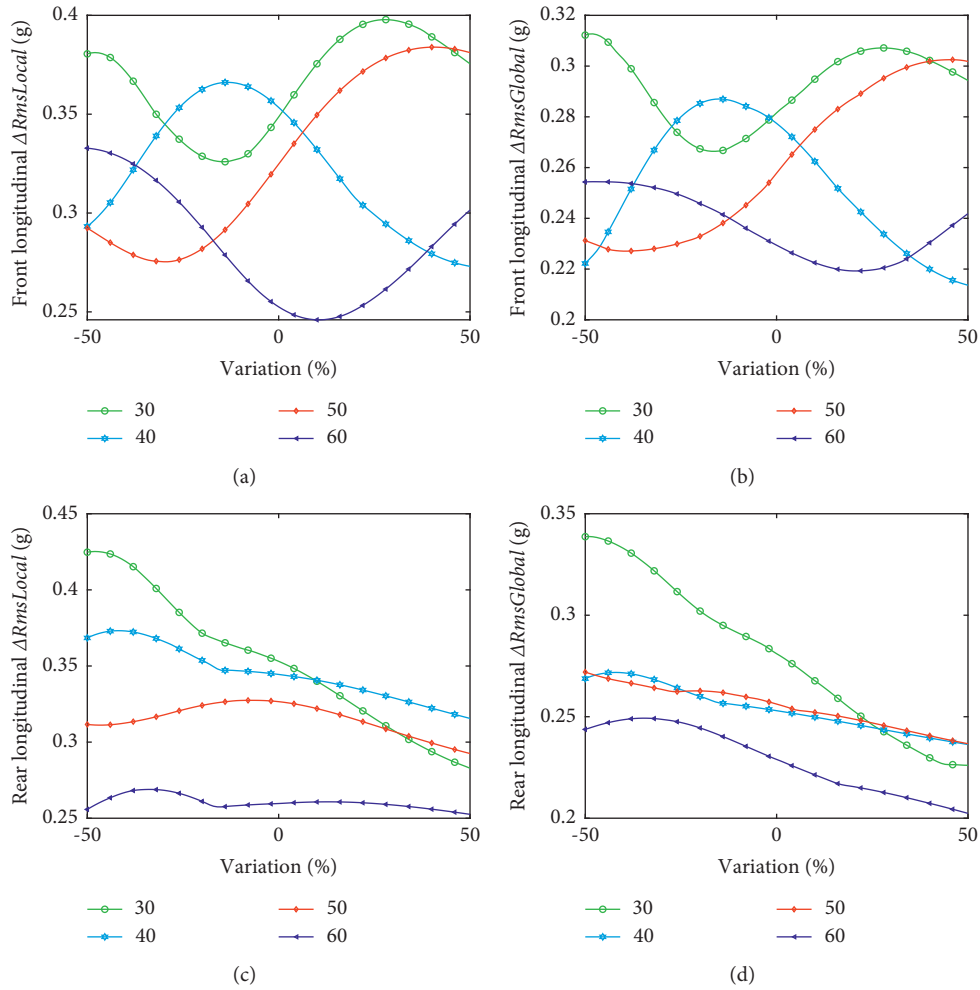

Figure 14: Trends of the indexes with bushing stiffness at different vehicle speeds: T_B^Y vs. front longitudinal ΔRmsLocal (a); T_B^Y vs. front longitudinal ΔRmsGlobal (b); T_{A4}^X vs. rear longitudinal ΔRmsLocal (c); T_{A4}^X vs. rear longitudinal ΔRmsGlobal (d).

where ΔRms$L1$ is the longitudinal ΔRmsLocal of the front seat rail; ΔRms$L2$ is the vertical ΔRmsLocal of the front seat rail; ΔRms$L3$ is the longitudinal ΔRmsLocal of the rear seat rail; ΔRms$L4$ is the vertical ΔRmsLocal of the rear seat rail; and $[f_{df}]$ and $[f_{dr}]$ are the allowable values of dynamic deflection of the front and rear suspensions, respectively. The values of $[f_{df}]$ and $[f_{dr}]$ in this paper are 50 mm and 30 mm, respectively.

5.2. Multiobjective Optimization Algorithm. The genetic algorithm is a group search algorithm that continuously finds and compares optimal solutions and eliminates poor solutions by iteratively simulating the process of biological evolution. NSGA-II is a more classical modern genetic algorithm that uses an elite retention strategy to better retain elite individuals, addressing the problem of standard genetic algorithms, where the last generation of individuals is discarded in the iteration [25]. In addition, it uses a fast nondominated ranking method to reduce computational complexity. The algorithm then reengages in the selection, crossover mutation, and elite retention until the maximum number of evolutionary generations is reached, at which point the Pareto frontier is obtained. Through the above analysis, this paper uses the NSGA-II algorithm to optimize the above multiobjective optimization problem. The main parameters of the NSGA-II algorithm optimization are shown in Table 4.

Table 4: Main parameters of NSGA-II algorithm.

Parameter	Value
Population size	12
Number of generations	20
Crossover probability	0.9
Mutation distribution index	20
Max failed runs	100
Failed run penalty	1000

5.3. Analysis of Optimization Results. Figure 15 shows the partial set of Pareto solutions obtained by the optimization algorithm at a vehicle speed of 30 km/h. Figure 15(a) shows the Pareto set of solutions for the RMS of the dynamic load on the front wheels with respect to the vertical ΔRmsLocal of the front seat rail. Figure 15(b) shows the Pareto set of

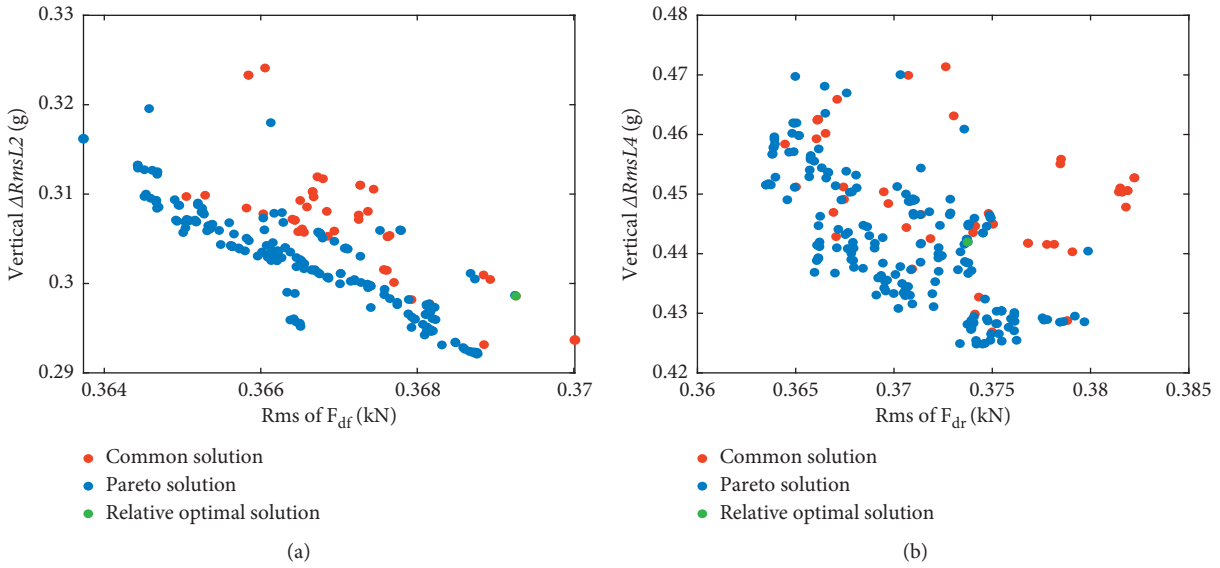

Figure 15: The projection of Pareto sets: onto dynamic loads Rms and vertical ΔRms$L1$ (a); onto dynamic loads Rms and vertical ΔRms$L4$ (b).

Table 5: Comparison of optimization results.

Parameters	Before optimization	After optimization	Percentage change (%)
ΔRms$L1$ (g)	0.354002543	0.249441268	−29.54
ΔRms$L2$ (g)	0.303106921	0.298594014	−1.49
ΔRms$L3$ (g)	0.353069798	0.248816026	−29.53
ΔRms$L4$ (g)	0.457749996	0.441953026	−3.45
F_{df} (kN)	0.367386372	0.369260841	0.51
F_{dr} (kN)	0.372544352	0.373740012	0.32
σ_p (g)	0.036960514	0.035220008	−4.71
K_{sf} (N/mm)	21	20.28365283	−3.41
B_{sf} (N·s/mm)	2.16	1.997156851	−7.54
K_{sr} (N/mm)	26	24.0494012	−7.50
B_{sr} (N·s/mm)	0.96	0.966029956	0.63
T_B^Y (N/mm)	332	278.4620487	−16.13
T_{A4}^X (N/mm)	330	494.462681	49.84

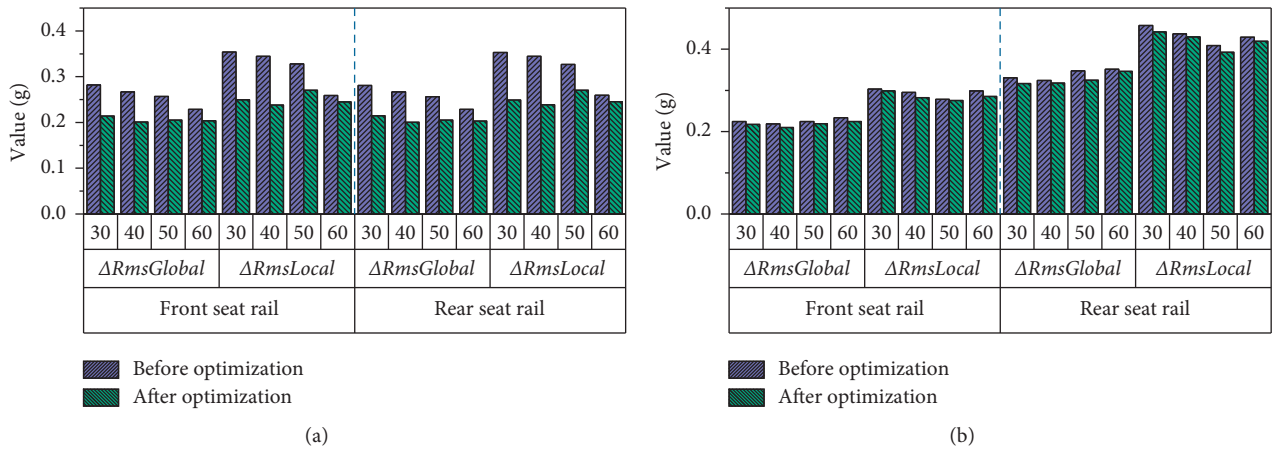

Figure 16: Comparison of results before and after optimization at different vehicle speeds: longitudinal (a); vertical (b).

Table 6: Results for optimized variables after optimization.

Parameters	30 km/h	40 km/h	50 km/h	60 km/h
K_{sf} (N/mm)	20.28365283	22.78026042	19.27164038	20.67443909
B_{sf} (N·s/mm)	1.997156851	1.947629857	1.94421668	1.947121335
K_{sr} (N/mm)	24.0494012	23.76412423	23.66549701	26.44512566
B_{sr} (N·s/mm)	0.966029956	0.913898048	0.928911581	0.895457426
K_{TY}^{B} (N/mm)	278.4620487	486.843411	301.8880437	376.3872639
$K_{TX}^{A_4}$ (N/mm)	494.462681	494.9839004	486.6719285	493.9985812

solutions for the RMS of the dynamic load on the rear wheels with respect to the vertical ΔRmsLocal of the rear seat rail. Table 5 shows the values of the optimization objectives and optimization variables before and after the optimization.

After optimization, the longitudinal ΔRmsLocal of the front seat rail decreases by 25.94% and the vertical ΔRmsLocal decreases by 1.49%. The longitudinal ΔRmsLocal of the rear seat rail decreases by 29.53% and the vertical ΔRmsLocal decreases by 3.45%. The RMS of the vehicle pitch angle acceleration decreases by 4.71%. The increase in the RMS value of the dynamic load of the front tyres was 0.51% and the increase in the RMS value of the dynamic load of the rear tyres was 0.32%. After optimization, the RMS of the dynamic loads on the front and rear tyres increased less and the safety of the vehicle could be guaranteed. In summary, the optimization has improved the vibration characteristics of the vehicle on bump road and the safety has not worsened.

The optimization is carried out at different vehicle speeds. The ΔRmsLocal and ΔRmsGlobal of both the longitudinal and vertical directions of the seat rail are obtained. The results of before and after optimization are shown in Figure 16. As can be seen from the graph, the values of ΔRmsLocal and ΔRmsGlobal of both the longitudinal and vertical directions of the front and rear seat rails are reduced after optimization. Table 6 shows the optimization results of the optimization variables for different vehicle speeds. As can be seen from the table, the values of the optimization variables that make the vehicle ride comfort better at each speed are different. The suspension parameters need to be matched reasonably to ensure the vehicle ride comfort.

6. Conclusions

In this study, the parameters of the MacPherson front suspension and the E-type multilink rear suspension are matched reasonably to enhance the vehicle ride comfort on bump road. The following conclusions are drawn:

(1) The longitudinal stiffness of the front suspension is influenced by the stiffness T_B^Y of the bushing B mostly. The longitudinal stiffness of the rear suspension is influenced by the stiffness T_{A4}^X of the bushing A_4 mostly.

(2) ΔRmsLocal and ΔRmsGlobal of the front and rear seat rails are used as the vibration evaluation indexes. The vertical ΔRmsLocal and ΔRmsGlobal of the seat rails are influenced by the stiffness of spring and the damping of the shock absorbers mostly. The longitudinal ΔRmsLocal and ΔRmsGlobal of the seat rails are influenced by the stiffness T_B^Y of the bushing B and the stiffness T_{A4}^X of the bushing A_4 mostly.

(3) The trends of ΔRmsLocal and ΔRmsGlobal with bushing stiffness are influenced by the speed of the vehicle.

(4) Optimal matching of suspension parameters by NSGA-II algorithm at different speeds: at the speed of 30 km/h, the longitudinal ΔRmsLocal and the vertical Δ*RmsLocal* of the front seat rail decrease by 25.94% and 1.49%, respectively. The longitudinal ΔRmsLocal and vertical ΔRmsLocal of the rear seat rail decrease by 29.53% and 3.45%, respectively. The other indexes are within reasonable range. The matching combination of suspension parameters that makes the vehicle ride comfort better is different at different vehicle speeds.

Data Availability

The data used to support the findings of this study are included within the article.

Conflicts of Interest

The authors declare that there are no conflicts of interest regarding the publication of this paper.

Acknowledgments

This project was supported by the National Natural Science Foundation of China (NSFC) (No. 51965026). The authors greatly appreciate this financial support.

References

[1] M. Wang, B. J. Zhang, Y. C. Chen, N. Zhang, and J. Zhang, "Frequency-based modeling of a vehicle fitted with Rollplane hydraulically interconnected suspension for ride comfort and experimental validation," *IEEE Access*, vol. 8, pp. 1091–1104, 2019.

[2] H. L. Guntur and L. F. Setiawan, "The influence of asymmetry ratio and average of the damping force on the performance and ride comfort of a vehicle," *International Journal of Vehicle Systems Modelling and Testing*, vol. 11, no. 2, pp. 97–115, 2016.

[3] Q. Chen, X. X. F. Bai, A. D. Zhu, D. Wu, X. C. Deng, and Z. D. Li, "Influence of balanced suspension on handling stability and ride comfort of off-road vehicle," *Proceedings of the Institution of Mechanical Engineers-Part D: Journal of Automobile Engineering*, vol. 235, no. 6, pp. 1602–1616, 2020.

[4] R. Jiao and V. Nguyen, "Studies on the low frequency vibration of the suspension system for heavy trucks under different operation conditions," *Noise and Vibration Worldwide*, vol. 52, no. 2, .2020.

[5] X. Zhou, Q. Zhang, and Z. Jin, "Study of suspension longitudinal frequency response characteristics," in *SAE 2-012*World Congress and Exhibition, Washington, DC, USA, 2012.

[6] X. Zhao, S. Wang, M. Yu, Q. Yu, and C. Y. Zhou, "The position of speed bump in front of truck scale based on vehicle vibration performance," *Journal of Intelligent and Fuzzy Systems*, vol. 34, no. 2, pp. 1083–1095, 2018.

[7] G. Verros, S. Natsiavas, and C. Papadimitriou, "Design optimization of quarter-car models with passive and semiactive suspensions under random road excitation," *Journal of Vibration and Control*, vol. 11, no. 5, pp. 581–606, 2005.

[8] H. Qi, Y. Chen, N. Zhang, B. Zhang, D. Wang, and B. Tan, "Improvement of both handling stability and ride comfort of a vehicle via coupled hydraulically interconnected suspension and electronic controlled air spring," *Proceedings of the Institution of Mechanical Engineers-Part D: Journal of Automobile Engineering*, vol. 234, no. 2-3, pp. 552–571, 2019.

[9] B. H. Tan, Y. Wu, N. Zhang, B. J. Zhang, and Y. C. Chen, "Improvement of ride quality for patient lying in ambulance with a new hydropneumatic suspension," *Advances in MEchanical Engineering*, vol. 11, no. 4, .2019.

[10] S. Ebrahimi-Nejad, M. Kheybari, and S. V. N. Borujerd, "Multiobjective optimization of a sports car suspension system using simplified quarter-car models," *Mechanics and Industry*, vol. 21, no. 4, 2020.

[11] J. Li, W. C. Guo, L. Wang, and S. S. Chen, "Multi-objective optimization of ambulance ride comfort under speed bump," *IEEJ Transactions on Electrical and Electronic EnginEering*, vol. 14, no. 6, pp. 1372–1380, 2019.

[12] M. M. S. Kaldas, K. Caliskan, R. Henze, and F. Kucukay, "Optimization of damper top mount characteristics to improve vehicle ride comfort and harshness," *Shock and Vibration*, vol. 2014, Article ID 248129, 15 pages, 2014.

[13] M. Aydin and Y. S. Unlusoy, "Optimization of suspension parameters to improve impact harshness of road vehicles," *International Journal of Advanced Manufacturing Technology*, vol. 60, no. 5–8, pp. 743–754, 2011.

[14] A. C. Mitra, M. V. Patil, and N. Banerjee, "Optimization of vehicle suspension parameters for ride comfort based on RSM," *Journal of the Institution of Engineers*, vol. 96, no. 2, pp. 165–173, 2015.

[15] V. S. V. Satyanarayana, B. Sateesh, and N. M. Rao, "Parameters optimisation of vehicle suspension system for better ride comfort," *Vehicle Performance*, vol. 4, no. 2, pp. 186–199, 2018.

[16] A. Jamali, H. Shams, and M. Fasihozaman, "Pareto multiobjective optimum design of vehicle-suspension system under random road excitations," *Proceedings of the Institution of Mechanical Engineers-Part K: Journal of Multibody Dynamics*, vol. 228, no. 3, pp. 282–293, 2014.

[17] D. Phu, V. Mien, P. H. T. Tu, N. P. Nguyen, and S. B. Choi, "A new optimal sliding mode controller with adjustable gains based on Bolza-Meyer criterion for vibration control," *Journal of Sound and Vibration*, vol. 485, 2020.

[18] S. L. He, K. R. Chen, E. Y. Xu, W. Wang, and Z. S. Jiang, "Commercial vehicle ride comfort optimization based on intelligent algorithms and nonlinear damping," *Shock and Vibration*, vol. 2019, Article ID 2973190, 16 pages, 2019.

[19] P. Choi, "A new adaptive fuzzy PID controller based on riccati-like equation with application to vibration control of vehicle seat suspension," *Applied Sciences*, vol. 9, no. 21, p. 4540, 2019.

[20] D. X. Phu and V. Mien, "Robust control for vibration control systems with dead-zone band and time delay under severe disturbance using adaptive fuzzy neural network," *Journal of the Franklin Institute-Engineering and Applied Mathematics*, vol. 357, no. 17, pp. 12281–12307, 2020.

[21] Z. Q. Guo, W. Wu, and S. H. Yuan, "Longitudinal-vertical dynamics of wheeled vehicle under off-road conditions," *Vehicle System Dynamics*, 2020.

[22] J. Hurel, J. Peralta, J. Amaya, B. Flores, and F. Flores, "Determination of the equivalent parameters for modelling a McPherson suspension with a quarter-car model," in *Proceedings of the 26th IEEE International Symposium on Industrial Electronics (ISIE)*, pp. 454–459, IEEE, Edinburgh, Scotland, June 2017.

[23] L. Tang, W. B. Shangguan, and L. Dai, "A calculation method of joint forces for a suspension considering nonline-ar elasticity of bushings," *Proceedings of the Institution of Mechanical Engineers-Part K: Journal of Multibody Dynamics*, vol. 226, no. K4, pp. 281–297, 2012.

[24] X. L. Wang, L. Dai, and W. B. Shangguan, "Calculation of joint forces of a multilink suspension for strength and fatigue analysis of bushings and control arms," *International Journal of Vehicle Design*, vol. 66, no. 3, pp. 217–234, 2014.

[25] W. Chunyan, Z. Yuqi, and Z. Wanzhong, "Multi-objective optimization of a steering system considering steering modality," *Advances in Engineering Software*, vol. 126, pp. 61–74, 2018.